Journal of Sound and Vibration 328 (2009) 156–190

Contents lists available at ScienceDirect

Journal of Sound and Vibration

journal homepage: www.elsevier.com/locate/jsvi

Total instability of turbocharger rotors—Physical explanation of the dynamic failure of rotors with full-floating ring bearings

Bernhard Schweizer *

Department of Mechanical Engineering, Multibody Systems, University of Kassel, Mönchebergstr. 7, 34109 Kassel, Germany

ARTICLE INFO

Article history:
Received 1 April 2008
Received in revised form
19 March 2009
Accepted 23 March 2009
Handling Editor: C.L. Morfey
Available online 21 August 2009

ABSTRACT

This article investigates the stability of turbocharger rotors with full-floating ring bearings. Rotors of turbochargers can show different bifurcations, when a control parameter—for instance rotor speed—is varied. Considering a rotor run-up, the rotor typically becomes unstable (first bifurcation) already at low rotor speeds and reaches a stable limit cycle (*1. Subsynchronous*). At higher rotor speeds, further bifurcations usually occur. For instance, the *1. Subsynchronous* can become unstable and the system bifurcates into another limit cycle (*2. Subsynchronous*, *3. Subsynchronous*). Also, limit cycles may collapse so that the rotor becomes stable again performing mere imbalance oscillations. Which bifurcations occur, depends on the rotor and bearing parameters. Since the limit cycle oscillations (*1.*, *2.* and *3. Subsynchronous*) are normally stable, i.e., the amplitudes (bearing eccentricities and rotor amplitudes) of the limit cycles are moderate, they do not impair safe operation of the turbocharger. Although the *Subsynchronous* vibrations may not interfere with the proper operation of the turbocharger, they can be undesirable, since they may cause acoustic noise problems, for instance.

Depending on the system parameters (rotor mass/inertia, shaft stiffness, bearing parameters, etc.) the rotor can, however, show a further kind of bifurcation and become totally unstable (dangerous high bearing eccentricities and rotor amplitudes), which in practice often leads to the destruction of the rotor. This phenomenon is called *Total Instability* in the present paper.

The article at hand examines a medium-sized turbocharger supported in full-floating ring bearings and analyses the bifurcation into *Total Instability*. The dynamics of the rotor/bearing system is investigated in detail and a sound physical explanation of the *Total Instability* is given. For this purpose, transient multibody simulations and eigenvalue calculations of the rotor/bearing system are carried out. In addition, a run-up measurement, which exhibits *Total Instability*, is compared with simulation results.

It is shown in this paper that bifurcation into *Total Instability* can physically be explained as synchronization of two limit cycles, namely as synchronization of the inner and outer *oil whirl/whip* of the floating ring bearings.

* Tel.: +49 561 804 3259; fax: +49 561 804 2847.
E-mail address: schweizer@mks.uni-kassel.de

0022-460X/$ - see front matter © 2009 Elsevier Ltd. All rights reserved.
doi:10.1016/j.jsv.2009.03.028

1. Introduction

Instabilities and bifurcations occurring in rotors supported with hydrodynamic bearings are often induced by the oil films and entail the well-known *oil whirl* and *oil whip* phenomena. Without or with less external damping, a rotor—e.g., a Laval rotor (see Appendix C)—could not be run in the unstable *oil whirl/whip* region, because bearing eccentricity ε would almost reach 1 (see Fig. 1(a), plot with damping $d_{ex} = 5$ Ns/m). If external damping is applied, e.g., a velocity-proportional damping force acting at the center of the rotor (see Appendix C), the oil-film induced instability leads to a limit cycle oscillation with moderate amplitudes, i.e., bearing eccentricities remain clearly less than 1 (see Fig. 1(a), plots with damping $d_{ex} = 30$ and 60 Ns/m). The higher the external damping, the smaller the orbit (bearing eccentricity ε) of the limit cycle is. If the external damping is high enough and if the parameters of the rotor/bearing system are properly chosen, the instability (*oil whirl/whip*) can be passed through and the rotor becomes stable again at higher rotor speeds, see Fig. 1(b).

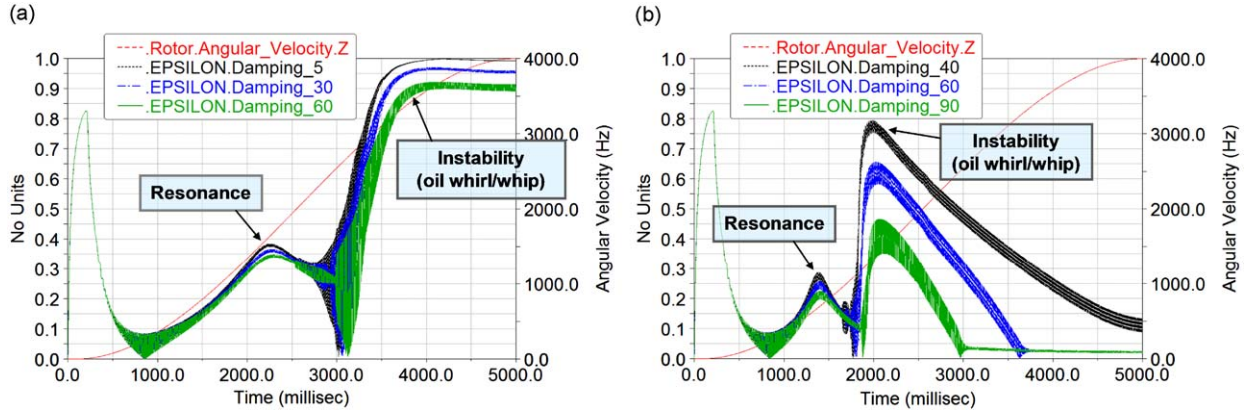

Fig. 1. Run-up simulations of a Laval rotor symmetrically supported in two plain hydrodynamic bearings; bearing eccentricity ε over time for two different stiff rotors and varying external damping: (a) Laval rotor (rotor eigenfrequency $\omega_{Eig} = \sqrt{c_{shaft}/m} = 1950$ Hz, imbalance $U_R = 0.4$ gmm) with external damping $d_{ex} = 5$, 30, 60 Ns/m and (b) Laval rotor (rotor eigenfrequency $\omega_{Eig} = \sqrt{c_{shaft}/m} = 710$ Hz, imbalance $U_R = 0.4$ gmm) with external damping $d_{ex} = 40$, 60, 90 Ns/m.

Because of the double oil film, rotors with full-floating ring bearings exhibit a more complex system behavior than rotors with single oil film bearings. Regarding full-floating ring bearings, both oil films—the inner and the outer oil film—may become unstable. Therefore, one observes *oil-whirl/whip* induced self-excited oscillations resulting from the inner and the outer oil film. Since the effective hydrodynamic angular velocity (see Appendix A) in the inner fluid film is higher than the effective hydrodynamic angular velocity in the outer fluid film when the rotor is in a stable equilibrium position, the inner fluid film is usually the first to become unstable.

A gyroscopic eigenvalue analysis of the linearized rotor/bearing system of a conventional turbocharger shows that the *first four normal modes* are approximately rigid body modes, namely the *gyroscopic conical backward* and the *gyroscopic conical forward mode* as well as the *gyroscopic translational backward* and the *gyroscopic translational forward mode* (see Appendix B.1). Note that under normal operating conditions, the backward modes are not or just slightly excited. In the examined turbocharger system, higher normal modes—for instance bending modes, see modes 6 and 7 in Appendix B.1—are not or just slightly excited in the observed speed range. Therefore, the *gyroscopic conical forward mode* and the *gyroscopic translational forward mode* are the mainly excited modes of the system.

Considering a turbocharger rotor in full-floating ring bearings, the inner and the outer fluid films of the left (compressor-sided) and right (turbine-sided) floating ring bearing can become unstable. This leads to *oil whirl/whip* instabilities in the inner and the outer fluid films with corresponding *whirl/whip* frequencies. The inner and the outer *whirl/whip* frequencies will excite the normal modes of the rotor/bearing system. So, basically four cases may be distinguished:

- The *oil whirl/whip* in the inner fluid film(s) excites the *gyroscopic conical forward mode* (the corresponding frequency in the spectrum cascade is called *1. Subsynchronous*).
- The *oil whirl/whip* in the inner fluid film(s) excites the *gyroscopic translational forward mode* (*2. Subsynchronous*).
- The *oil whirl/whip* in the outer fluid film(s) excites the *gyroscopic conical forward mode* (*3. Subsynchronous*).
- The *oil whirl/whip* in the outer fluid film(s) excites the *gyroscopic translational forward mode* (*4. Subsynchronous*).

Turbochargers running under normal operating conditions—i.e., rotor speed is below the threshold speed for *Total Instability*—only exhibit the *1., 2.* and *3. Subsynchronous*. We are not aware of any measurements or simulations that show the *4. Subsynchronous*, although occurrence of the *4. Subsynchronous* is theoretically possible.

Besides the self-excited oscillations (*1., 2.* and *3. Subsynchronous*) mentioned above, the system can reach a further limit cycle, which is called *Total Instability* in this paper. It will be shown in Section 3 that *Total Instability* is caused by the synchronization of two limit cycle oscillations: The inner and the outer *oil whirl/whip* synchronize and the synchronized *whirl/whip* frequency excites a natural mode of the rotor system (*gyroscopic forward mode 2 of Appendix B.2*). Due to the *whirl/whip* synchronization, the (mutual) damping of the inner and outer oil films is significantly reduced. This results in almost circular inner and outer *whirl/whip* orbits with inner and outer bearing eccentricities $\varepsilon_{i,o}$ close to 1.

Hence, for safely operating turbochargers, mainly four frequencies will be detected in spectrum cascades of rotor run-ups (also multiples, fractions and combinations of these four frequencies due to system nonlinearities [1]):

- The *Synchronous* (due to rotor imbalance).
- The *1. Subsynchronous* (*oil whirl/whip* in the inner fluid film excites the *gyroscopic conical forward mode*; the outer fluid film damps the inner *oil whirl/whip*).
- The *2. Subsynchronous* (*oil whirl/whip* in the inner fluid film excites the *gyroscopic translational forward mode*; the outer fluid film damps the inner *oil whirl/whip*).
- The *3. Subsynchronous* (*oil whirl/whip* in the outer fluid film excites the *gyroscopic conical forward mode*; the inner fluid film damps the outer *oil whirl/whip*).

Since the inner *oil whirl/whip* is damped by the outer oil films and vice versa, the inner and outer bearing eccentricities $\varepsilon_{i,o}$ usually remain well below 1 during oscillation in the *1., 2.* and *3. Subsynchronous*. Which of the three *Subsynchronous* occur in the frequency spectrum and at which rotor speed they arise, depends on the parameters of the rotor/bearing system (rotor mass/inertia, shaft stiffness, bearing parameters, etc.).

In the following, a typical bifurcation sequence (see Fig. 3(c)), often observed in turbocharger run-ups, is described:

(I) At low rotor speeds, the rotor is stable and performs imbalance vibrations (*Synchronous*) around a stable equilibrium position.

(II) When the rotor speed is increased, the inner fluid films become unstable and excite the *gyroscopic conical forward mode*. The rotor reaches a stable limit cycle (*1. Subsynchronous*). The amplitudes of the *1. Subsynchronous* are moderate: Due to the damping of the outer fluid films, the bearing eccentricities ε_i of the inner fluid films remain clearly <1.

(III) When the rotor speed is further increased, a second bifurcation emerges. The first limit cycle (*1. Subsynchronous*) becomes unstable and the rotor bifurcates into a second limit cycle (*2. Subsynchronous*), i.e., the inner fluid films remain unstable, but they now excite the *gyroscopic translational forward mode*. In other words, the system jumps from the *gyroscopic conical forward mode* into the *gyroscopic translational forward mode*.

(IV) Increasing rotor speed even further leads to a third bifurcation. The *2. Subsynchronous* disappears and the system becomes stable again (only *Synchronous*). Thus, the *oil whirl/whip* instability of the inner fluid films is passed through.

(V) Again increasing rotor speed, a fourth bifurcation occurs. Now, the outer fluid films become unstable and excite the *gyroscopic conical forward mode*. The rotor reaches a stable limit cycle (*3. Subsynchronous*). The amplitudes of the *3. Subsynchronous* are moderate: Due to the damping of the inner fluid films, the outer bearing eccentricities ε_o remain clearly <1.

Remark 1. It is also possible that the *2. Subsynchronous* and the *3. Subsynchronous* occur simultaneously (stable limit cycle oscillation with two *Subsynchronous* and moderate amplitudes), see Fig. 2. In this case, inner and outer *oil whirl/whip* occur simultaneously. The system is, however, not totally unstable, since the inner and the outer *whirl/whip* frequency are different, so that the inner and the outer oil films can damp each other sufficiently (mutual damping due to $\dot{\varepsilon}_{i,o}$ and $\dot{\delta}_{i,o}$ movement, see Appendix A.3).

Remark 2. The *2. Subsynchronous* and *3. Subsynchronous* may be apparent up to the maximum operating speed. Somtimes, however, the instabilities can be passed through, i.e., the *Subsynchronous* will disappear at high rotor speeds. In this case, the rotor becomes again stable and performs imbalance vibrations around a stable equilibrium position (see Figs. 2 and 3(b, d, e)).

In addition to the bifurcation scenario described above, various other bifurcation sequences are observed in measurements and simulations. Some typical bifurcation scenarios are qualitatively illustrated in Fig. 3.

It should be mentioned that the simultaneous appearance of two *subsynchronous whirl/whip* frequencies in rotor systems (see above Remark 1) is well known in literature. In Ref. [2], the coexistence of two lateral modes of an isotropic rotor has been reported. The coupled motion of two neighboring shafts has been investigated in Ref. [3], where the coexistence of two *whirl/whip* frequencies resulting from the instabilities of two coupled shafts is examined. Also, a coupling effect is discussed, which resembles the *Total Instability* of turbochargers in full-floating ring bearings.

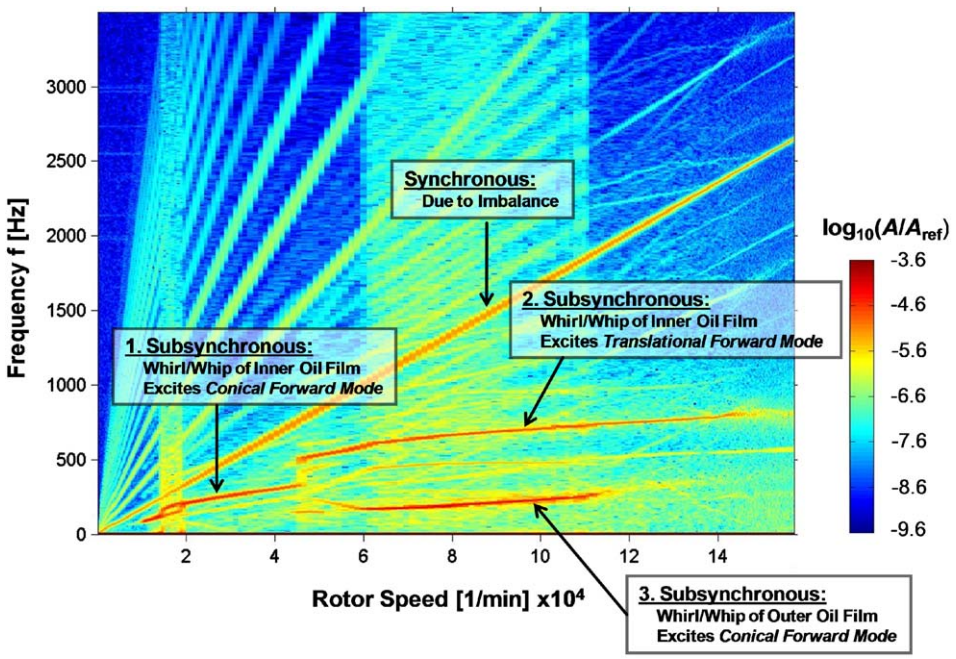

Fig. 2. Spectrum cascade (displacement of compressor-sided shaft extension) measured during a rotor run-up of an automotive turbocharger [1].

General remark on the use of the term "limit cycle" in this paper: The term "limit cycle" is normally used only for self-excited motions of autonomous systems (e.g., rotor balanced perfectly). The notions "*subsynchronous whirl/whip*" or "*non-synchronous whirl/whip*" are frequently used for self-excited motions of non-autonomous systems (e.g., rotor with imbalance), see Refs. [3,4]. In the present paper, we use the term "limit cycle" generally for self-excited motions of non-autonomous systems, i.e., also for quasiperiodic oscillations.

Early works on the stability of rotors in hydrodynamic journal bearings based on simple rotor/bearing models can be found in Refs. [5–8]. Fundamental theoretical analyses on the *oil whirl* and *oil whip* phenomena are carried out in Refs. [9–11]. A detailed survey on experimental and theoretical works concerning the stability of rotors in hydrodynamic bearings is given in Ref. [4]. The influence of external damping on the stability of a Laval rotor is, for instance, discussed in Refs. [12,13].

Linear stability analyses for a Laval rotor in full-floating ring bearings have, e.g., been carried out in Refs. [14,15]; ring speed measurements can be found in Refs. [16,17]. Bifurcations occurring in Laval rotor systems with full-floating ring bearings are investigated in Ref. [18]. Run-up measurements and corresponding simulations as well as a detailed review on recent works on turbocharger rotors with floating ring bearings can be found in Refs. [19–21].

In order to analyze the bifurcation behavior of the rotor/bearing system, only run-up simulations are performed in this work. Because of the system's complexity, no analytical stability and bifurcation calculations are accomplished. A theoretical overview on nonlinear vibration effects occurring in dynamical systems—like the here investigated turbocharger system—can be found in Refs. [22,23], stability and bifurcations are treated, for instance, in Ref. [24]. Bifurcation analyses in connection with rotors in plain hydrodynamic bearings and full-floating ring bearings are carried out in Refs. [25–27].

This paper is structured as follows: In Section 2, the rotor model is introduced. Five run-up simulations are presented in Section 3. On the basis of these simulations and the eigenvalue calculations in Appendix B, the physical effects leading to the *Total Instability* are explained. In Section 4, a test-rig measurement, which exhibits *Total Instability* is presented. The paper is concluded in Section 5. In Appendix A, some basic geometrical properties concerning full-floating ring bearings are summarized. Results of three gyroscopic eigenfrequency analyses for the examined turbocharger rotor, are collected in Appendix B. Investigations on the stability behavior of a Laval (Jeffcott) rotor supported in plain hydrodynamic journal bearings and in full-floating ring bearings are carried out in Appendix C.

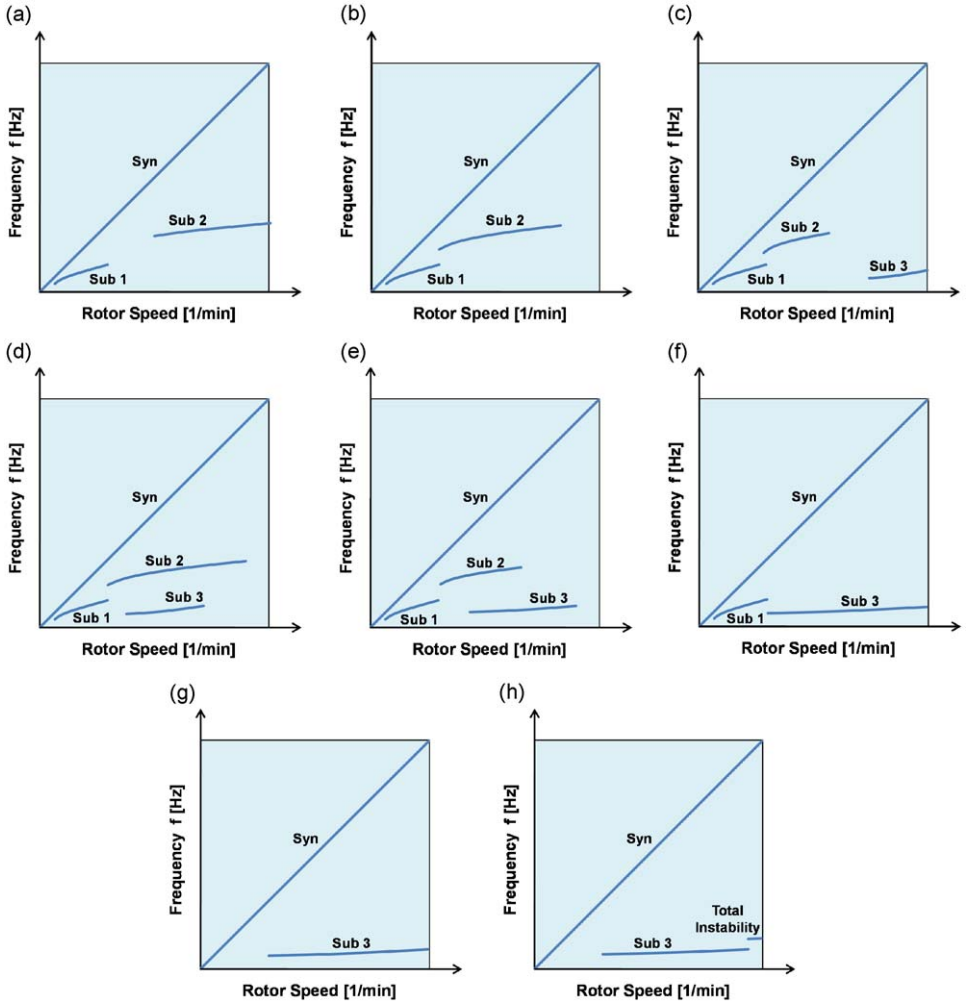

Fig. 3. Sketches of eight basic bifurcation sequences often observed in turbocharger run-ups (Syn = *Synchronous*, Sub 1 = *1. Subsynchronous*, etc.): (a) Sub 1, intermittent stabilization, Sub 2, (b) Sub 1 and Sub 2, Sub 2 is passed through, (c) Sub 1, Sub 2, intermittent stabilization and Sub 3, (d) Sub 1, Sub 2 and at same time Sub 3, (e) Sub 1, Sub 2 and at same time Sub 3, (f) Sub 1 and Sub 3, (g) Sub 3 (Sub 1 not or only slightly) and (h) Sub 3 and *Total Instability* (Sub 1 not or only slightly).

2. Rotor/bearing model of the turbocharger

The turbocharger rotor examined in this work consists of a rotor shaft, a compressor wheel, and a turbine wheel. A sketch of the rotor/bearing system is depicted in Fig. 4. Both wheels are fixed to the shaft. The imbalance of the two wheels is illustrated by two point masses. The rotor is supported in two full-floating ring bearings. To investigate the rotor vibrations and bifurcations, the vertical displacement (y-displacement) of the measurement point is analyzed.

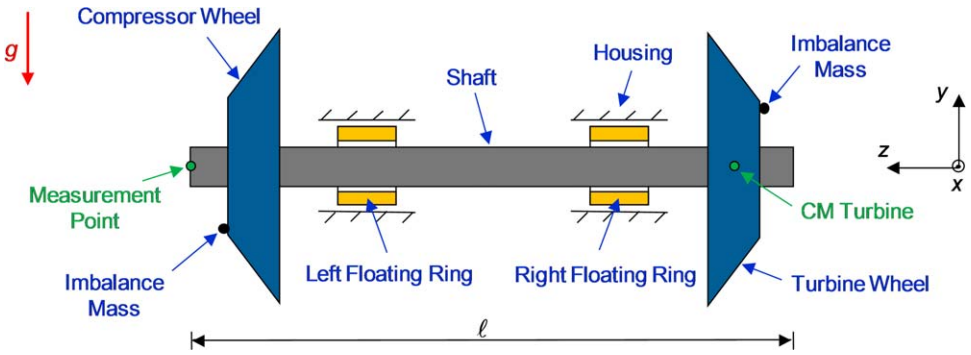

Fig. 4. Basic design of a turbocharger rotor.

For simulating turbocharger run-ups, a flexible multibody model [28] of the rotor/bearing system has been created. In this paper, a medium-sized turbocharger is examined. Some general data concerning the rotor are itemized below:

- Rotor length: $\ell \approx 300\,\text{mm}$
- Rotor mass: $m \approx 2.5\,\text{kg}$
- Dynamic oil viscosity (at 20 °C): $\eta \approx 0.2\,\text{Ns/m}^2$
- Imbalance turbine/compressor wheel (Simulation 1): $U_T \approx 7.0\,\text{gmm}/U_C \approx 2.5\,\text{gmm}$
- Considered speed range: $0 \leqslant \omega_{\text{Rotor}} \leqslant 1400\,\text{Hz}$
- Oil supply pressure: $p_{\text{sup}} \approx 4\,\text{bar}$
- Oil supply temperature: $T_{\text{sup}} \approx 90\,°\text{C}$

Rotor dynamics and rotor stability are mainly influenced by the floating ring bearings, i.e., by the oil flow and pressure generation in the inner and outer oil gap of the bearings. For calculating the pressure distribution in the oil gaps, Reynolds equation [29,30] is used. In this work, we assume an isothermal fluid flow; inertia effects, turbulence and misalignment are neglected. Reynolds equation is solved for the pressure field in the inner and outer oil gap by a finite element approach. With the pressure field, the resultant fluid film forces and friction torques can be calculated depending on position and velocity of rotor journal and floating ring. Fluid film forces and friction torques are implemented into the multibody model via look-up tables.

In the multibody model of the turbocharger, housing elasticity is taken into account by means of two linear springs, acting in the x- and y-direction with spring constants $c_{\text{housing},x}$ and $c_{\text{housing},y}$. Housing damping is simply modeled by linear dampers with damper constants $d_{\text{housing},x}$ and $d_{\text{housing},y}$, arranged parallel to the springs, see Fig. 5.

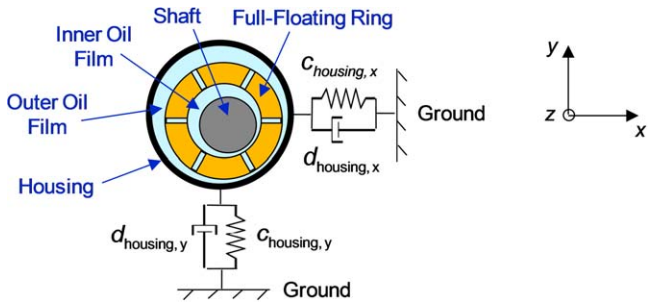

Fig. 5. Cross section through full-floating ring bearing: elastically bedded housing, ring and shaft.

The rotor shaft is discretized by finite elements, see Fig. 6(a), and incorporated into the multibody system using component mode synthesis [31], see Fig. 6(b). Compressor and turbine wheel—both modeled as rigid bodies—are

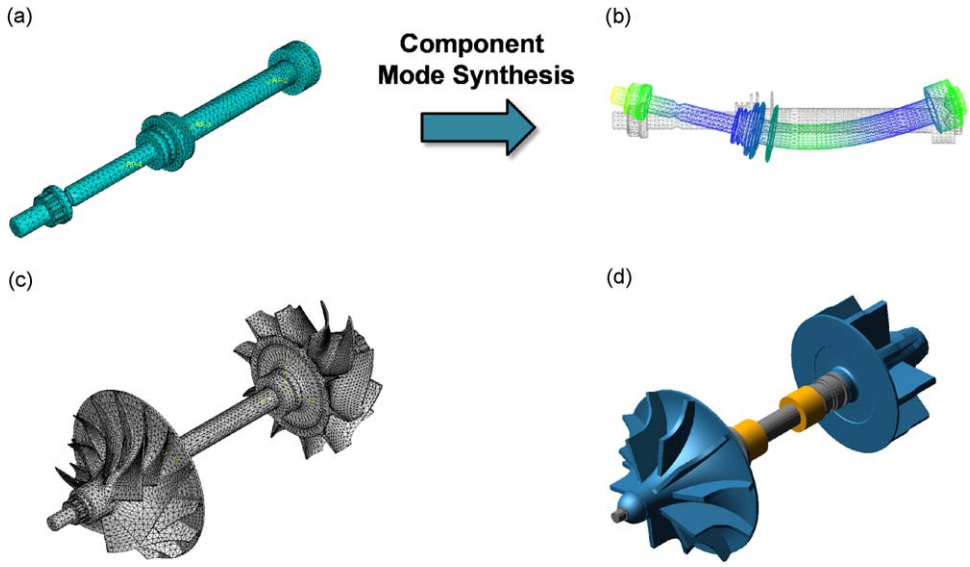

Fig. 6. (a) Finite element model of rotor shaft, (b) modally reduced rotor shaft, (c) finite element model of complete rotor and (d) multibody model of turbocharger.

appropriately attached to the shaft. The accuracy of the modally reduced rotor model was checked by an eigenvalue analysis of the fully discretized rotor, see Fig. 6(c), and also by an experimental modal analysis.

The two floating rings are modeled as rigid bodies able to perform translational and rotational motions. They are driven by the friction torque of the inner fluid films and retarded by the friction torque of the outer fluid films. The model does not consider any axial forces, e.g., due to axial thrust, and has no axial bearing. The complete multibody model is shown in Fig. 6(d).

3. Simulation results

Five run-up simulations with different system parameters have been carried out in order to illustrate and explain the bifurcations occurring in turbocharger systems.

- In Simulations 1 and 2, the rotor does not reach *Total Instability* within the considered speed range.
- Simulations 3, 4 and 5 exhibit *Total Instability*.
- Simulation 3 almost shows the measured instability frequency (≈ 280 Hz) and also the correct vibration mode (*gyroscopic forward mode 2 of Appendix B.2*), obviously because housing stiffness has been chosen properly.
- In Simulation 4, housing stiffness has evidently been assumed too high, so that the instability frequency in the region of *Total Instability* is too high (≈ 400 Hz). Also, the vibration mode is not correct (*gyroscopic forward mode 2 of Appendix B.3* instead of *gyroscopic forward mode 2 of Appendix B.2*).
- In Simulation 5, housing stiffness has been assumed too low with the consequence that the instability frequency is too low (≈ 250 Hz), although the mode shape is correct (*gyroscopic forward mode 2 of Appendix B.2*).

Parameters of the rotor/bearing system for the five run-up simulations are collected in Table 1, which shows the percentage changes relative to Simulation 1 (reference simulation).

Table 1
Simulation parameters.

	Sim 1 (%) (reference)	Sim 2 (%)	Sim 3 (%)	Sim 4 (%)	Sim 5 (%)
Inner bearing width B_i	100	–	–	–	–
Outer bearing width B_o	100	–	75	75	75
Inner bearing clearance ψ_i	100	–	145	145	145
Outer bearing clearance ψ_o	100	120	175	175	175
Housing stiffness c_{housing}	100	–	–	1100	33
Imbalance turbine U_T	100	–	190	115	220
Imbalance compressor U_C	100	–	–	–	180

3.1. Simulation 1 (reference simulation)

In Simulation 1, the rotor exhibits the *Synchronous*, the *1. Subsynchronous* and the *2. Subsynchronous*; the rotor does not reach *Total Instability* in the considered speed range. Fig. 7(a) shows the vertical vibration of the compressor-sided shaft extension (y-displacement of measurement point in Fig. 4) and also the y-displacement of the turbine wheel's center of mass (blue line); the green line represents rotor speed, which is steadily increased from 50 Hz up to 1400 Hz. The corresponding waterfall diagram of the vertical vibration of the measurement point is depicted in Fig. 7(b) and (c). The bifurcation sequence corresponds with Fig. 3(b). Which fluid films become unstable, can be seen regarding the inner/outer bearing eccentricities $\varepsilon_{l\_i}/\varepsilon_{l\_o}$ and $\varepsilon_{r\_i}/\varepsilon_{r\_o}$ of the left (compressor-sided) and right (turbine-sided) floating ring bearing in Fig. 7(d)–(e) as well as the effective hydrodynamic angular velocities $\omega_{\text{eff\_}l\_i}/\omega_{\text{eff\_}l\_o}$ and $\omega_{\text{eff\_}r\_i}/\omega_{\text{eff\_}r\_o}$ in Fig. 7(f)–(i).

- Up to $t \approx 1200$ ms, the rotor is stable and performs imbalance vibrations (*Synchronous*) around a stable equilibrium position.
- At $t \approx 1200$ ms, the inner oil films—in particular the inner oil film of the left bearing—become unstable (large increase in ε_i, $\omega_{\text{eff\_}i} \approx 0$ at the onset of the instability) and the system reaches a stable limit cycle. The *oil whirl/whip* frequency of the inner oil films excites the *gyroscopic conical forward mode* (*1. Subsynchronous*).
- The inner fluid films are stable again at $t \approx 2600$ ms.
- At $t \approx 3000$ ms, the inner fluid films—in particular the inner oil film of the left bearing—become unstable again, but now they excite the *gyroscopic translational forward mode* (*2. Subsynchronous*).
- At $t \approx 5500$ ms, the inner fluid films become stable again, the instability is passed through and the system (mainly) performs imbalance vibrations (*Synchronous*) about a stable equilibrium position (concerning the exact definition of fluid film instability, note the corresponding remark in Appendix C.1).

It should be mentioned that the high peaks in the plots of $\omega_{\text{eff\_}i,o}$ result from the singularity of $\omega_{\text{eff\_}i,o}$ for $\varepsilon_{i,o} = 0$ (see Appendix A).

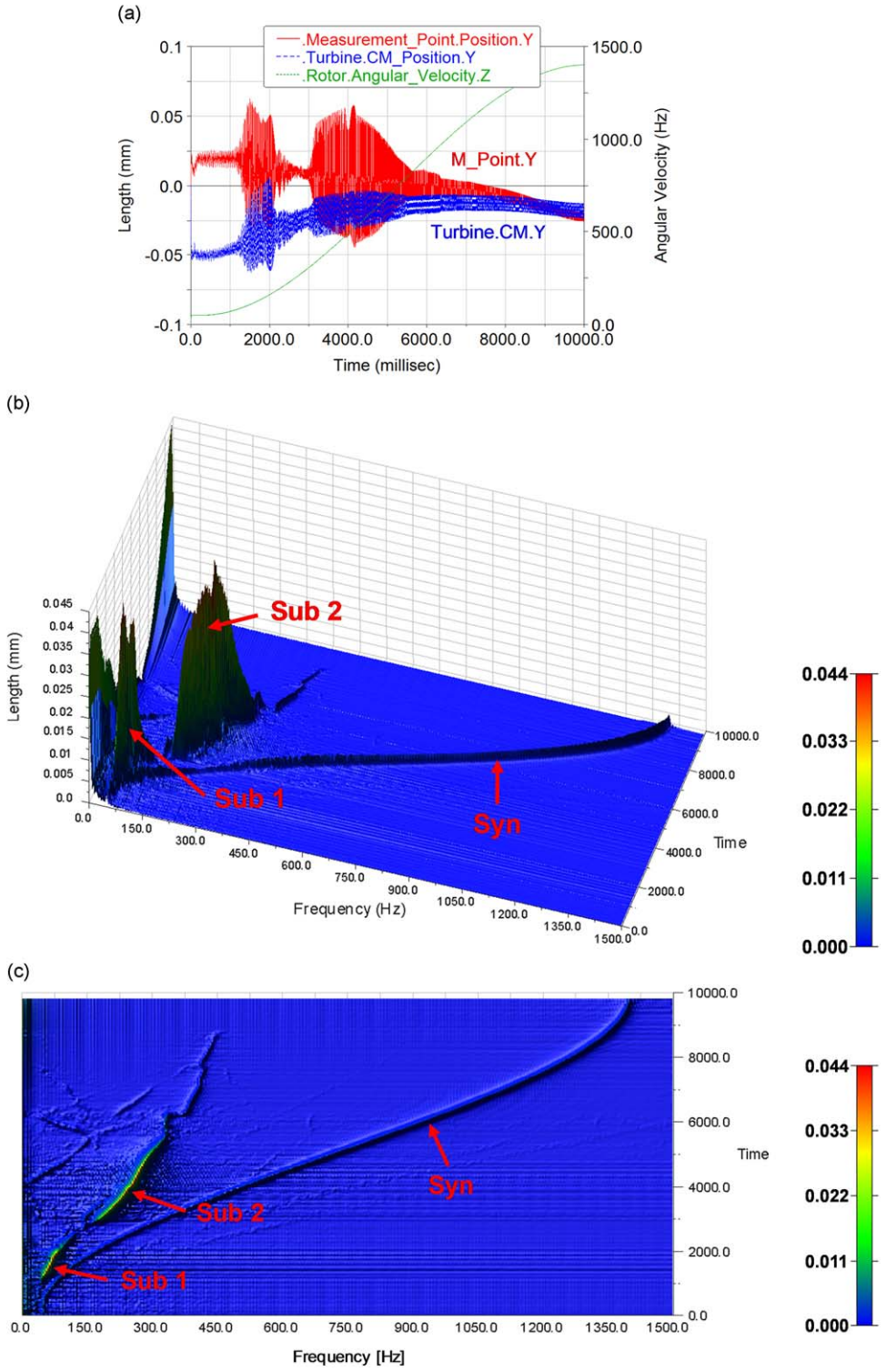

Fig. 7. Run-up Simulation 1: (a) *y*-displacement of measurement point (red) and CM turbine wheel (blue), rotor angular velocity (green), (b) 3D-waterfall diagram of plot (a), (c) top-view waterfall diagram, (d, e) bearing eccentricities and (f)–(i) effective hydrodynamic angular velocities. (For interpretation of the references to the color in this figure legend, the reader is referred to the web version of this article.)

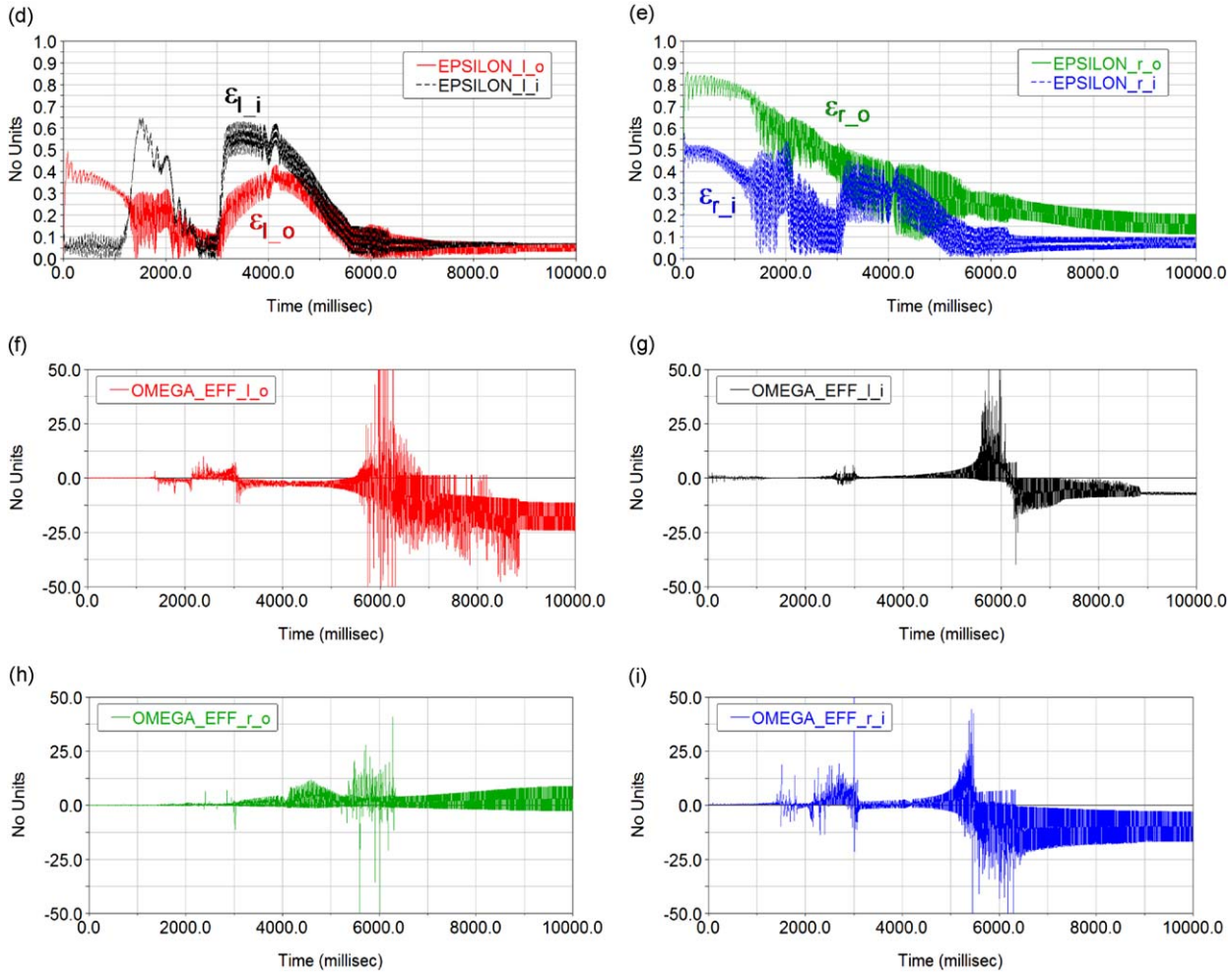

Fig. 7. (*Continued*)

3.2. Simulation 2

Compared to Simulation 1, the radial clearance ψ_o of the outer oil gap is increased by 20%. In Simulation 2 (Fig. 8), the rotor shows the *Synchronous*, the *1. Subsynchronous*, the *2. Subsynchronous* and the *3. Subsynchronous*; the rotor does not reach *Total Instability* in the observed speed range. The bifurcation sequence correlates with Fig. 3(c).

- The rotor is stable and vibrates around a stable equilibrium position (*Synchronous*) up to $t \approx 1200$ ms.
- The inner oil film(s)—primarily the inner oil film of the left bearing—become(s) unstable at $t \approx 1200$ ms and the rotor reaches the *1. Subsynchronous*.
- The inner fluid films are stable again at $t \approx 2100$ ms.
- At $t \approx 2900$ ms, the inner fluid films become unstable again and the rotor reaches the *2. Subsynchronous*.
- The inner fluid films are stable again at $t \approx 4300$ ms and the rotor performs mere imbalance vibrations (*Synchronous*).
- At $t \approx 8000$ ms, the outer oil films becomes unstable (large increase and large amplitudes in ε_o (especially ε_{r_o}), ω_{eff_o} oscillating around zero). The rotor reaches a stable limit cycle (*3. Subsynchronous*), where the *oil whirl/whip* frequency of the outer oil films excites the *gyroscopic conical forward mode*.

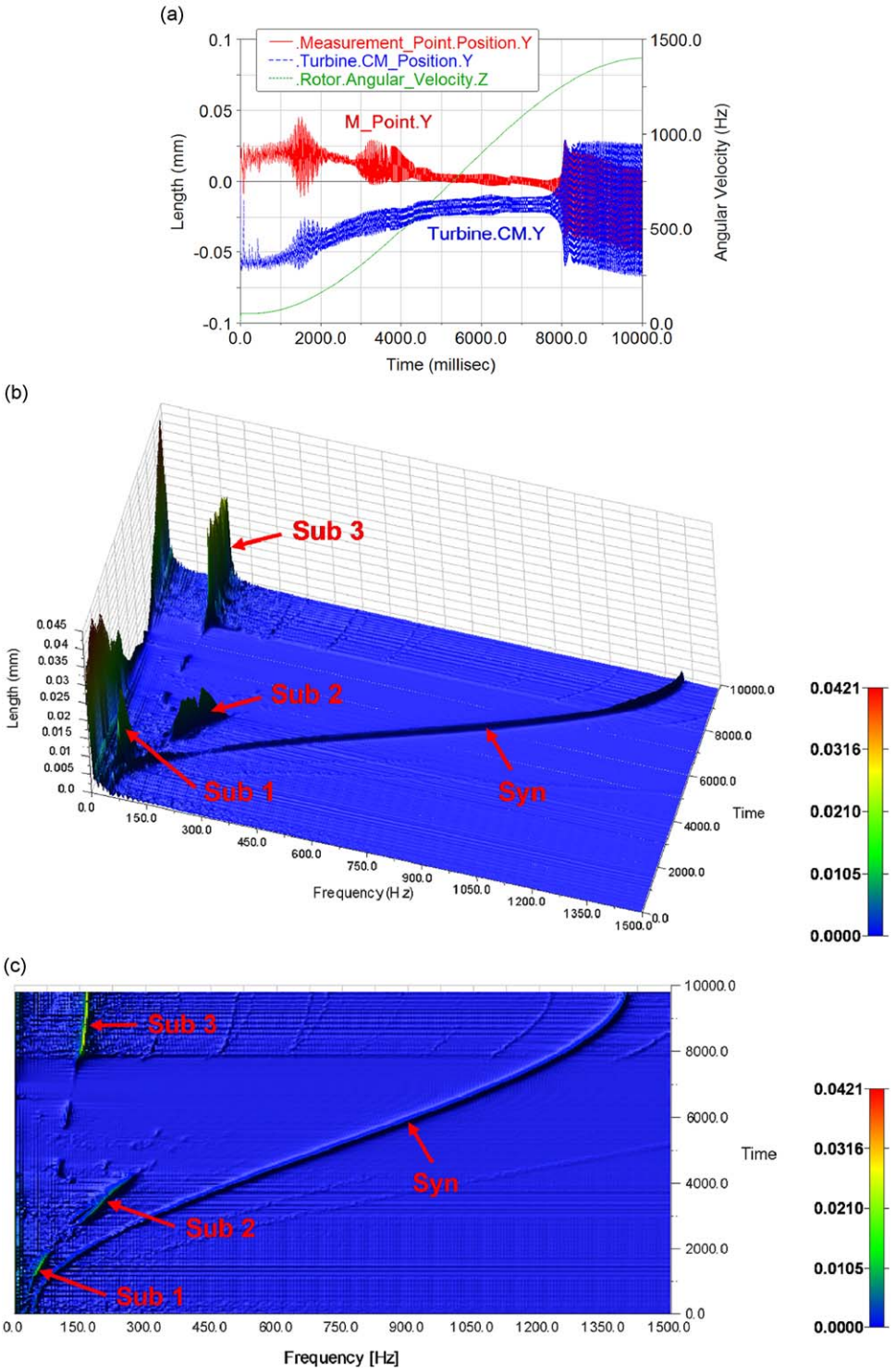

Fig. 8. Run-up Simulation 2: (a) *y*-displacement of measurement point (red) and CM turbine wheel (blue), rotor angular velocity (green), (b) 3D-waterfall diagram of plot (a), (c) top-view waterfall diagram, (d, e) bearing eccentricities, (f)–(i) effective hydrodynamic angular velocities. (For interpretation of the references to the color in this figure legend, the reader is referred to the web version of this article.)

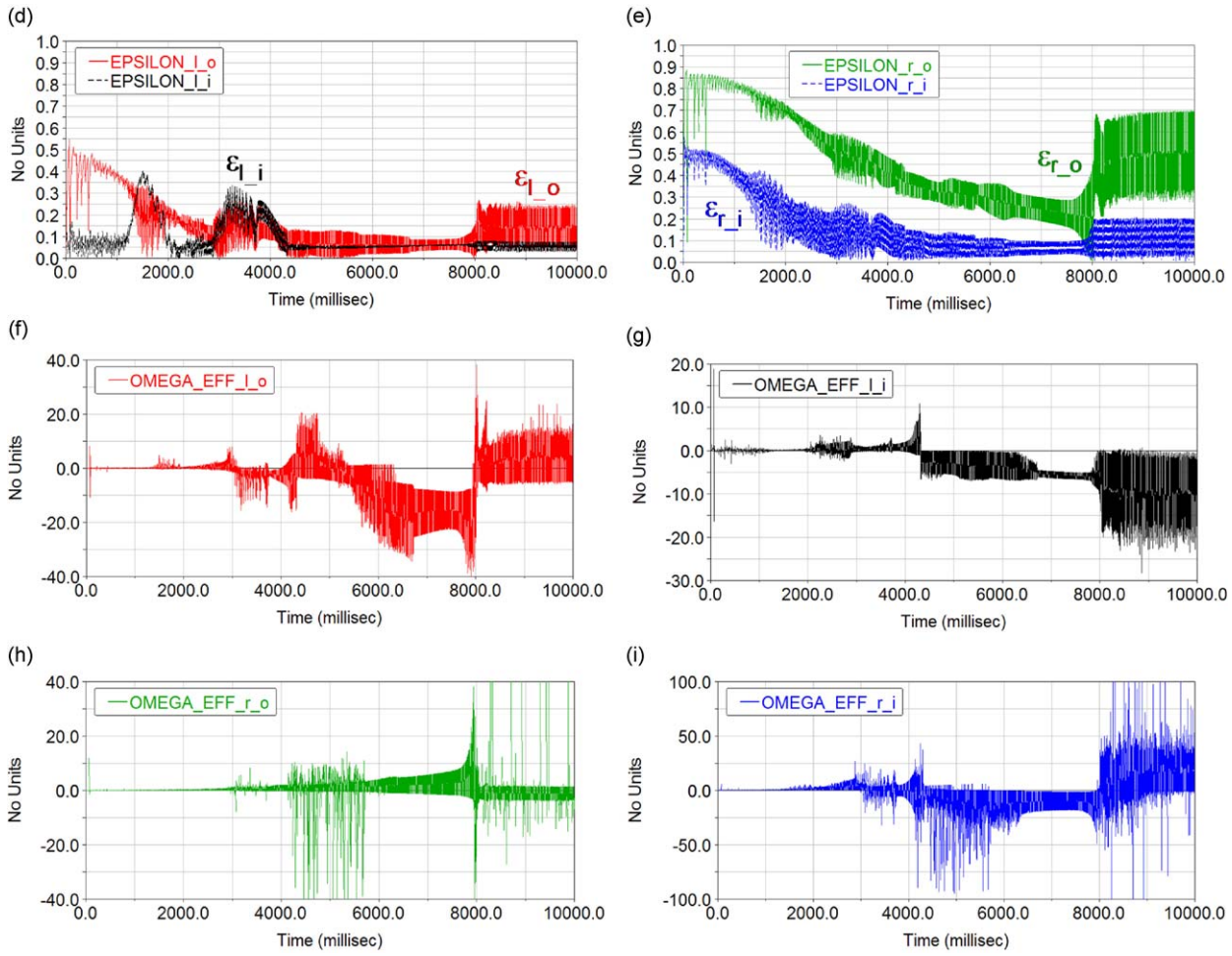

Fig. 8. (*Continued*)

3.3. Simulation 3

In contrast to Simulation 1, the width B_o of the outer oil gap is reduced by 25%, the outer clearance ψ_o is increased by 75% and the inner clearance ψ_i is increased by 45%. Furthermore, imbalance U_T at the turbine wheel is increased by 90%. As in the previous two simulations, housing stiffness is assumed to be $c_{\text{housing},x} = c_{\text{housing},y} = 3\text{E}4\,\text{N/mm}$ and housing damping is chosen by $d_{\text{housing},x} = d_{\text{housing},y} = 200\,\text{Ns/m}$. In Simulation 3 (Fig. 9), the rotor exhibits the *Synchronous* and the *3. Subsynchronous*; the rotor reaches *Total Instability*. The bifurcation sequence coincides with Fig. 3(h).

- Up to $t \approx 3500$ ms, the rotor performs imbalance vibrations (*Synchronous*) around a stable equilibrium. The imbalance oscillations are superimposed by transient oscillations due to the setting process at the beginning of the simulation.
- The outer oil films become unstable at $t \approx 3500$ ms and the system bifurcates into the *3. Subsynchronous*.
- At $t \approx 8700$ ms, *Total Instability* is reached.

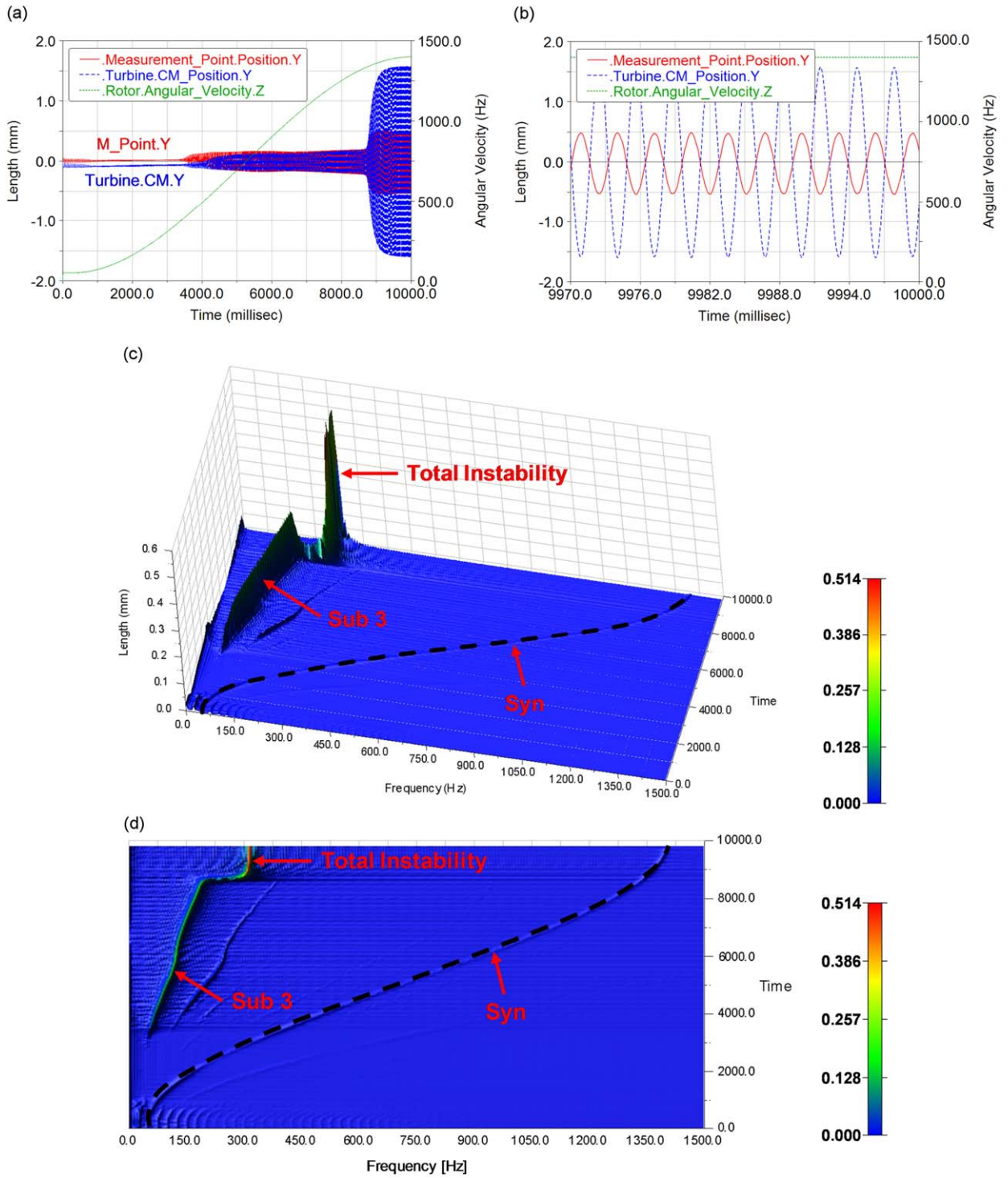

Fig. 9. Run-up Simulation 3: (a) *y*-displacement of measurement point (red) and CM turbine wheel (blue), rotor angular velocity (green), (b) detail of (a), (c) 3D-waterfall diagram of plot (a), (d) top-view waterfall diagram, (e, f) bearing eccentricities and (g)–(j) effective hydrodynamic angular velocities. (For interpretation of the references to the color in this figure legend, the reader is referred to the web version of this article.)

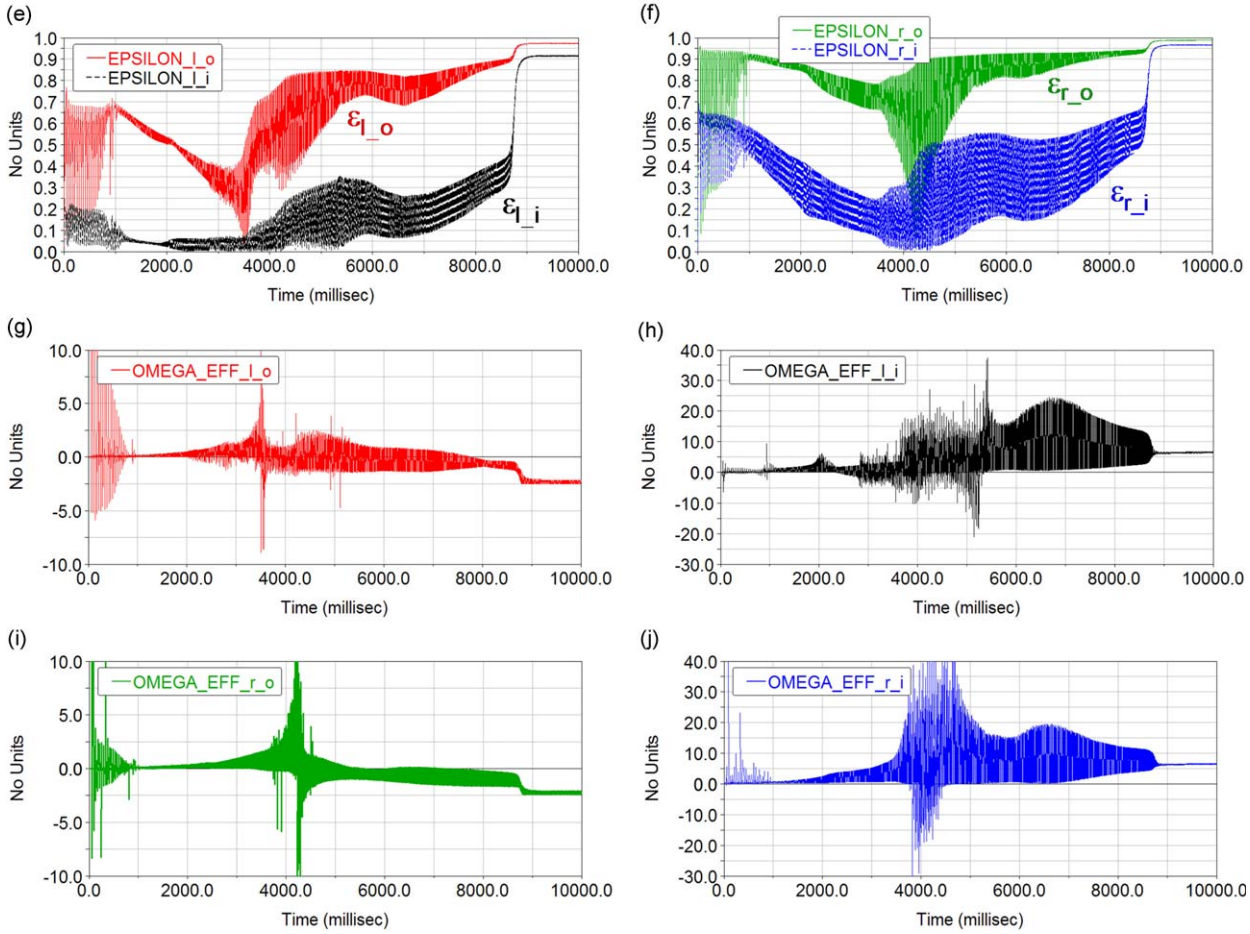

Fig. 9. (*Continued*)

Prior to bifurcation into *Total Instability*, one observes:

- With increasing rotor speed, the mean values of the inner and outer bearing eccentricities $\varepsilon_{i,o}$ steadily increase, but the amplitudes of $\varepsilon_{i,o}$ steadily decrease. On the other hand, in Simulation 2, the mean values and amplitudes of $\varepsilon_{i,o}$ remain almost constant when the rotor vibrates in the *3. Subsynchronous*.
- At the beginning of the *3. Subsynchronous*, the effective hydrodynamic angular velocities $\omega_{\text{eff\_}o}$ of the outer fluid films oscillate approximately around zero (see, e.g., plots for $\omega_{\text{eff\_}o}$ at $t \approx 5000$ ms); the mean values of the effective hydrodynamic angular velocities of the inner fluid films $\omega_{\text{eff\_}i}$ are greater than zero and have larger amplitudes. When the rotor speed is increased, the mean values of $\omega_{\text{eff\_}o}$ steadily decrease; also the amplitudes of $\omega_{\text{eff\_}i}$ continuously decrease.
- Due to the increasing inner and outer bearing eccentricities, the stiffness of the fluid films is continuously increased. Also, the fluid film damping behavior becomes increasingly "harder".

The onset of *Total Instability* is characterized by the following:

- A large, almost instantaneous increase (jump) of the rotor amplitudes and bearing eccentricities $\varepsilon_{i,o}$ (especially large increase in ε_i) is observed. Also, one detects a strong reduction of the amplitudes of the effective hydrodynamic angular velocities $\omega_{\text{eff\_}i,o}$ (especially $\omega_{\text{eff\_}i}$) and a clear jump of the mean values of $\omega_{\text{eff\_}o}$.
- The system jumps from the *gyroscopic conical forward mode* (*3. Subsynchronous*) into the *gyroscopic forward mode 2 of Appendix B.2 (Total Instability)* with an instability frequency of ≈ 300 Hz.
- *Total Instability* is induced when the inner fluid films become unstable (large increase in ε_i indicates the onset of the instability of the inner fluid films) so that now inner and outer fluid films are simultaneously unstable. The inner and the outer *whirl/whip* synchronize and excite both the *gyroscopic forward mode 2 of Appendix B.2*. Due to this synchronization, the mutual damping between the inner and outer oil films is strongly reduced (reduced $\dot{\varepsilon}_{i,o}$ and $\dot{\delta}_{i,o}$ damping) [18].
- When the inner and outer oil films are both unstable and excite the same mode (*gyroscopic forward mode 2 of Appendix B.2*), this mode frequency is too large for the nominal outer *whirl* frequency and too small for the nominal inner *whirl* frequency. Consequently, neither $\omega_{\text{eff\_}i} = 0$, nor $\omega_{\text{eff\_}o} = 0$. In the region of *Total Instability*, $\omega_{\text{eff\_}i} > 0$ and $\omega_{\text{eff\_}o} < 0$. Note that the nominal *whirl* frequency of the inner fluid film is $\approx 0.5 \cdot (\omega_J + \omega_R)$ and the nominal *whirl* frequency of the outer fluid film is $\approx 0.5 \cdot \omega_R$ (see Appendix A.2).
- In the region of *Total Instability*, $\omega_{\text{eff\_}i} > 0$ so that the inner fluid films drive the rotor. $\omega_{\text{eff\_}o} < 0$, i.e., the outer fluid films damp the (almost circular) rotor movement.

3.4. Simulation 4

In comparison with Simulation 3, imbalance of turbine wheel U_T is decreased by 75%. Compared with Simulations 1–3, housing stiffness is increased to $c_{\text{housing},x} = c_{\text{housing},y} = 3.5\text{E}5$ N/mm (almost rigid bearing housing). The results of Simulation 4 are shown in Fig. 10. The rotor exhibits the *Synchronous* and the *3. Subsynchronous*; the rotor reaches *Total Instability*. The bifurcation sequence corresponds to Fig. 3(h).

- Stable imbalance oscillations (*Synchronous*) are detected up to $t \approx 3600$ ms.
- The outer oil films become unstable at $t \approx 3600$ ms (*3. Subsynchronous*).
- The rotor reaches *Total Instability* at $t \approx 9150$ ms.

The bifurcation behavior is quite similar to Simulation 3. The main differences to Simulation 3 are:

- The rotor does not bifurcate into the *gyroscopic forward mode 2 of Appendix B.2*, but into the *gyroscopic forward mode 2 of Appendix B.3* , see Fig. 10(b), because of the increased housing stiffness. This means that the instability frequency is too high (≈ 400 Hz) compared to the measurement in Section 4. Therefore, taking housing stiffness into account properly allows to correctly simulate mode shape and frequency in the *Total Instability*.
- The bearing eccentricities are larger in the region of *Total Instability* than in Simulation 3 (apart from ε_{l_o}). Trend: The higher the housing stiffness, the higher the bearing eccentricities.
- Compared with Simulation 3, the threshold speed for reaching *Total Instability* is increased, mainly because of the reduced imbalance.

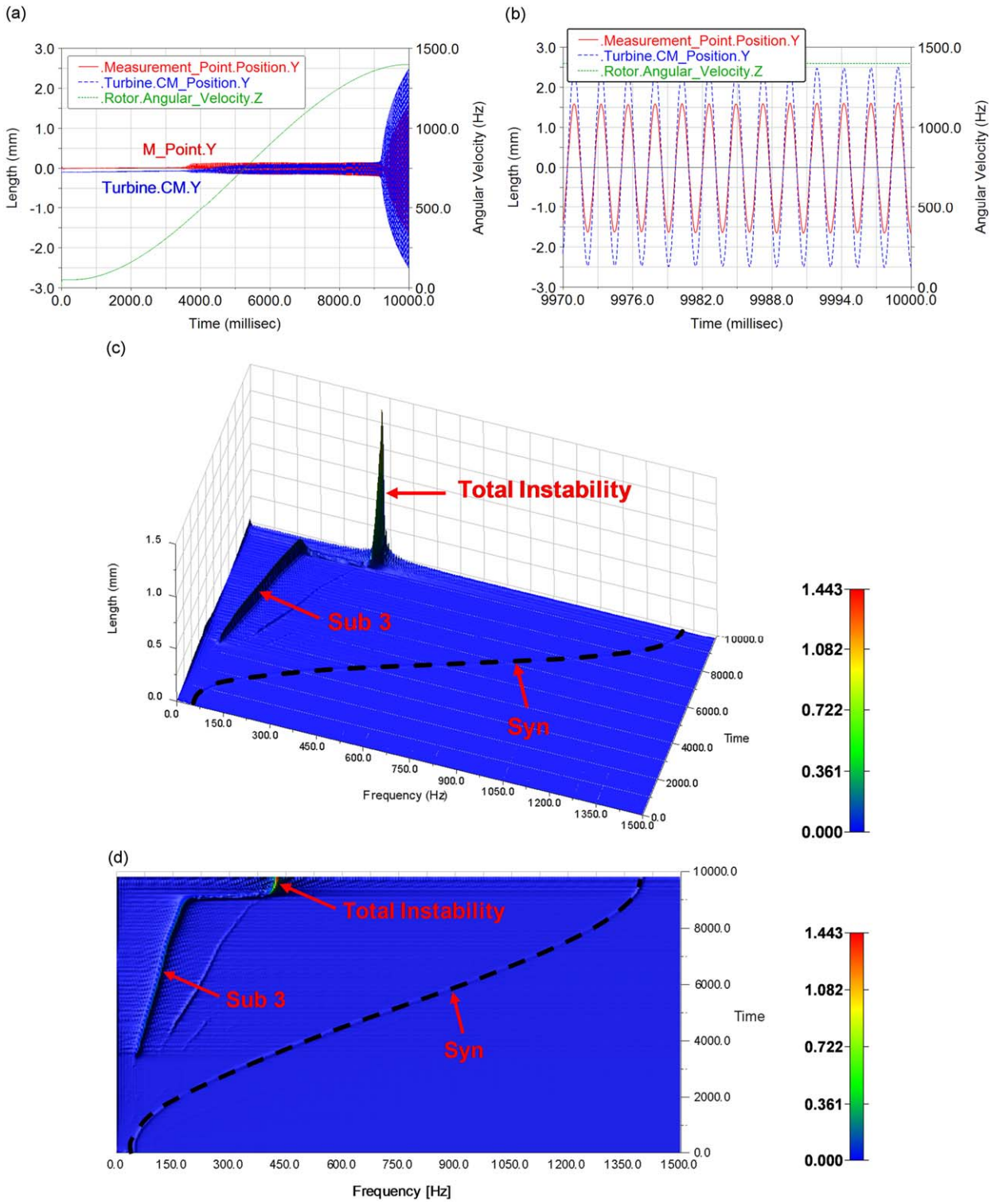

Fig. 10. Run-up Simulation 4: (a) *y*-displacement of measurement point (red) and CM turbine wheel (blue), rotor angular velocity (green), (b) detail of (a), (c) 3D-waterfall diagram of plot (a), (d) top-view waterfall diagram, (e, f) bearing eccentricities and (g)–(j) effective hydrodynamic angular velocities. (For interpretation of the references to the color in this figure legend, the reader is referred to the web version of this article.)

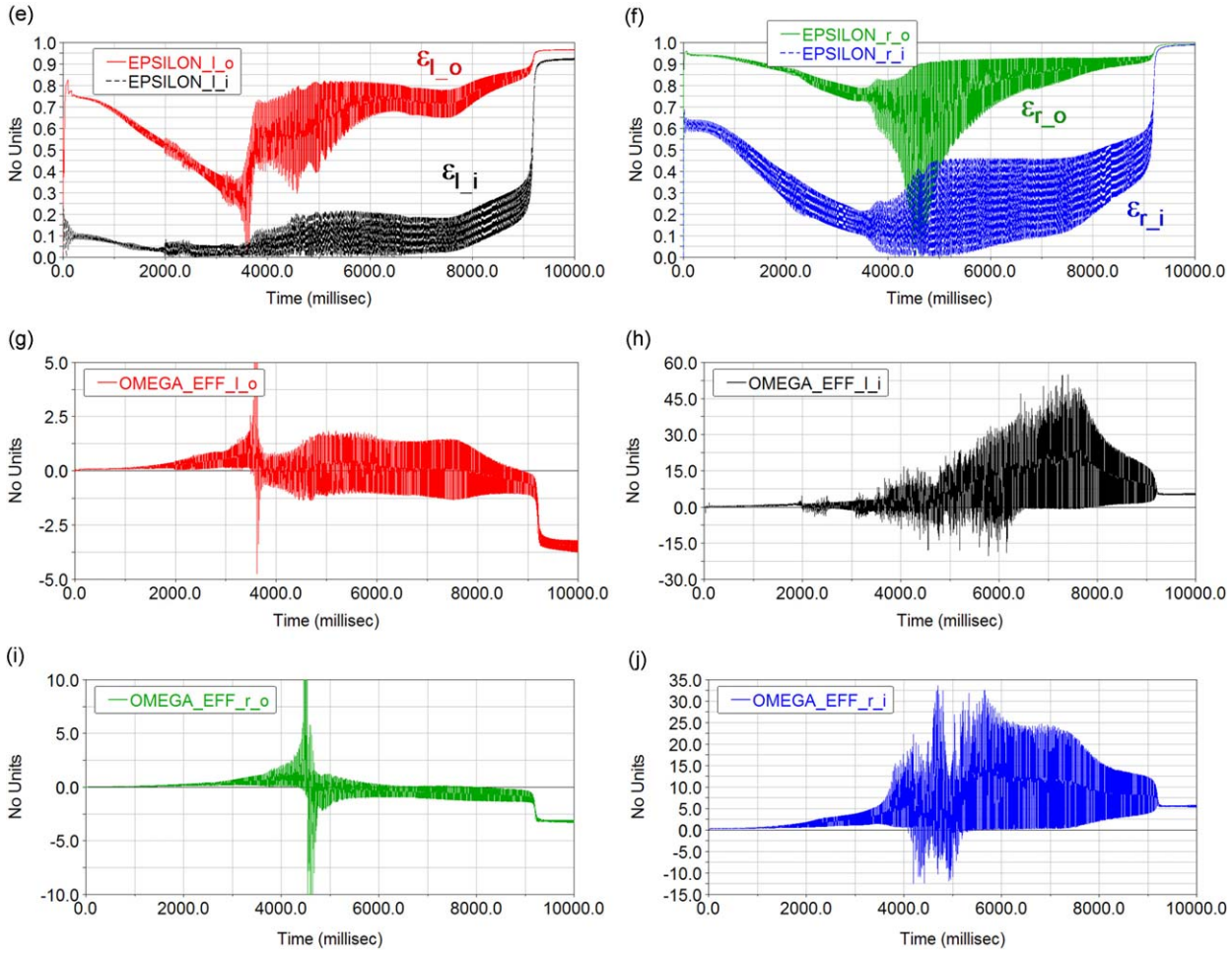

Fig. 10. (*Continued*)

3.5. Simulation 5

In contrast to Simulation 3, imbalances U_C and U_T at the compressor and turbine wheel are both increased (see Table 1). Housing stiffness is decreased to $c_{\text{housing},x} = c_{\text{housing},y} = 1.0\text{E}4\,\text{N/mm}$. The results of Simulation 5 are summarized in Fig. 11. The bifurcation sequence agrees again with Fig. 3(h).

- Up to $t \approx 4300\,\text{ms}$, one only observes imbalance oscillations (*Synchronous*), superimposed by transient oscillations due to the setting process at the beginning of the simulation.
- At $t \approx 4300\,\text{ms}$, the rotor bifurcates into the *3. Subsynchronous*.
- *Total Instability* is reached at $t \approx 8200\,\text{ms}$.

The bifurcation sequence resembles Simulation 3. The main differences compared with Simulation 3 are:

- Although the rotor bifurcates into the *gyroscopic forward mode 2 of Appendix B.2*, see Fig. 11(b), instability frequency is too low ($\approx 220\,\text{Hz}$) compared with the measurement in Section 4 due to the reduced housing stiffness.
- The bearing eccentricities $\varepsilon_{i,o}$ are less than in Simulation 3 and clearly <1 in the region of the *Total Instability*.
- Compared with Simulation 3, the threshold speed for reaching *Total Instability* is decreased, mainly because of the increased imbalances.

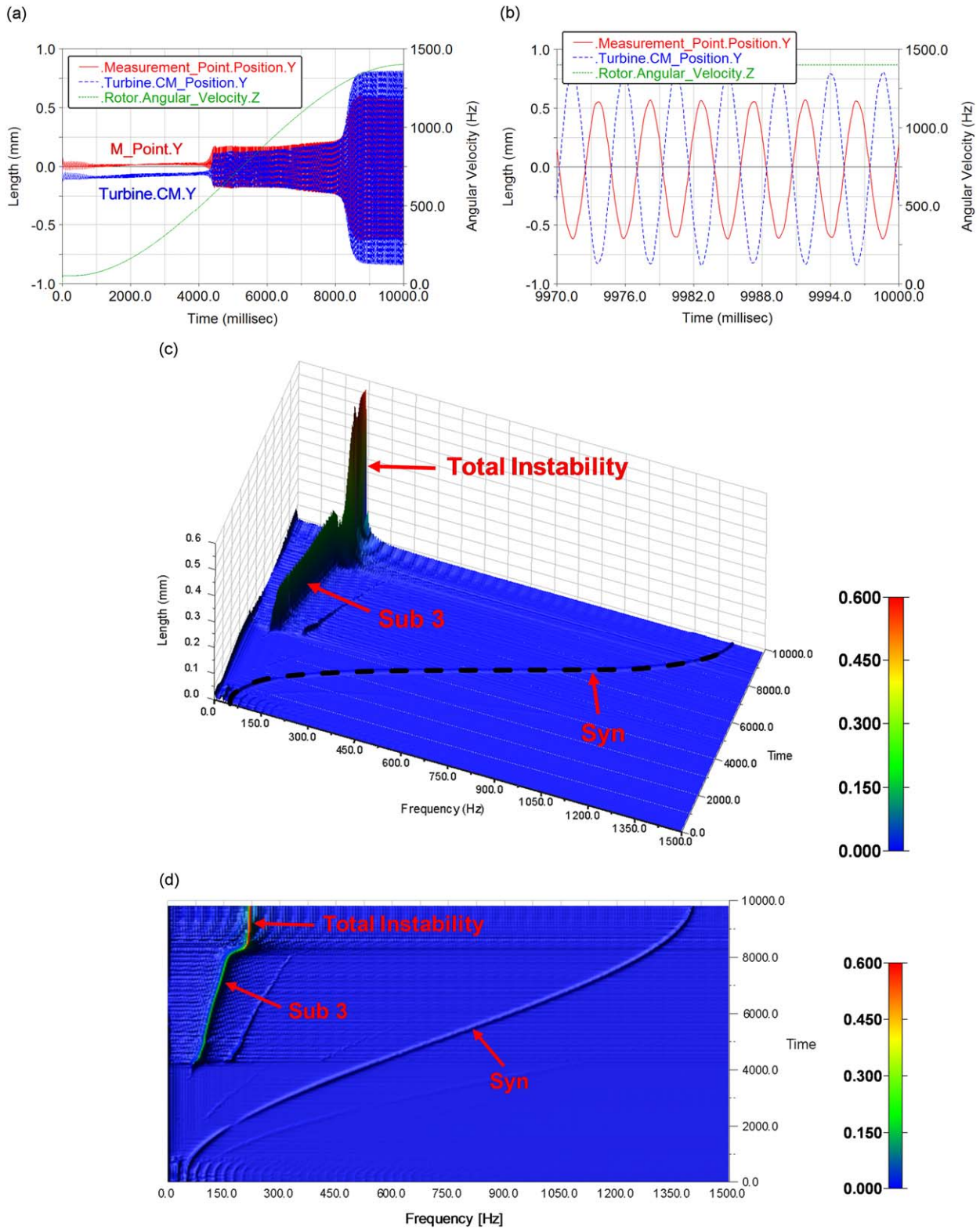

Fig. 11. Run-up Simulation 5: (a) *y*-displacement of measurement point (red) and CM turbine wheel (blue), rotor angular velocity (green), (b) detail of (a), (c) 3D-waterfall diagram of plot (a), (d) top-view waterfall diagram, (e, f) bearing eccentricities and (g)–(j) effective hydrodynamic angular velocities. (For interpretation of the references to the color in this figure legend, the reader is referred to the web version of this article.)

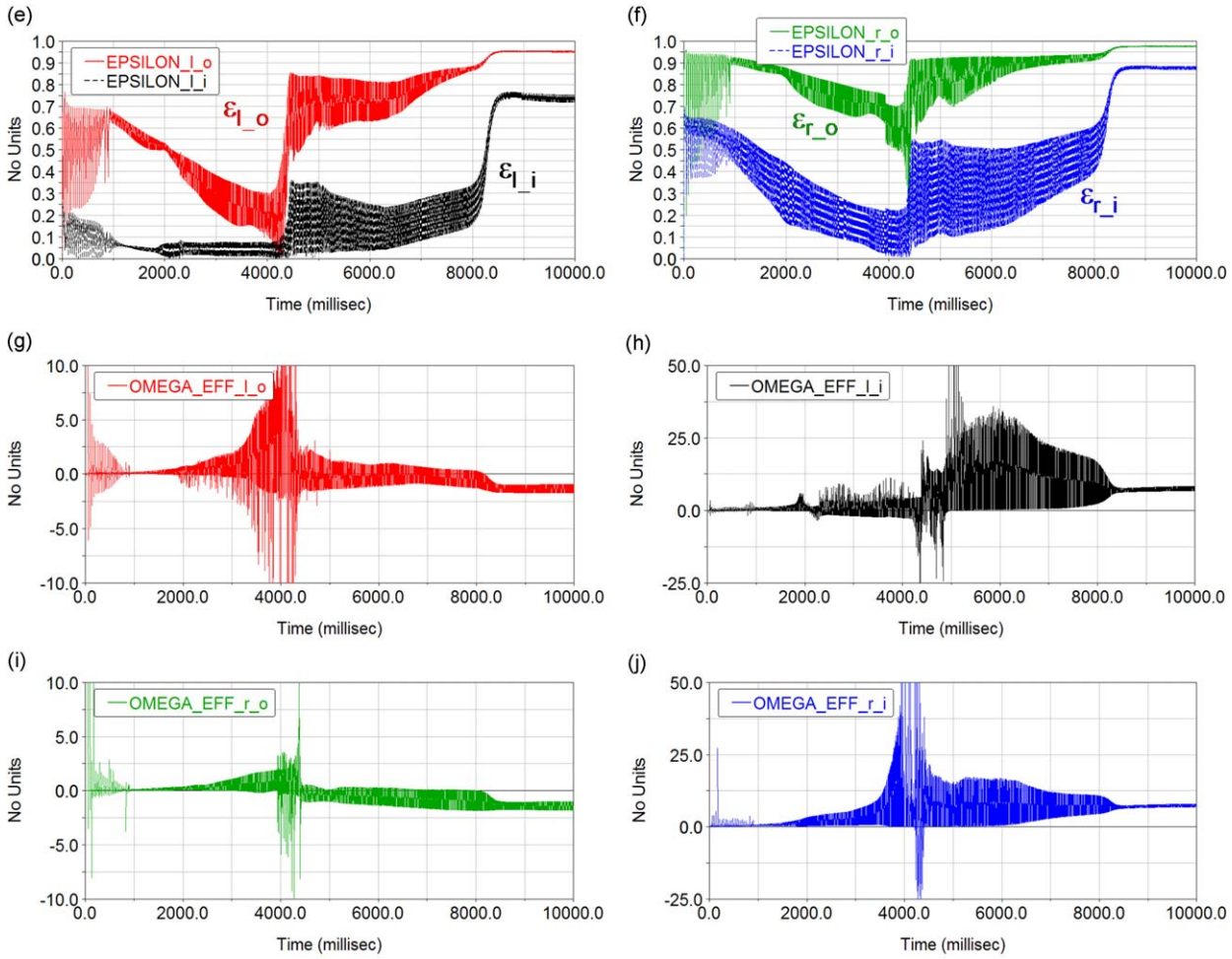

Fig. 11. (*Continued*)

3.6. *Discussion of simulation results*

The presented and further simulations with the current rotor show that the threshold speed for reaching *Total Instability* is decreased by

- increasing the outer bearing clearance ψ_o,
- decreasing the outer bearing width B_o,
- increasing the inner bearing width B_i,
- increasing the imbalance or by
- decreasing the oil supply pressure.

Simulations 3–5 exhibit *Total Instability*. The basic transition into *Total Instability* is the same in all three calculations. One can draw several general conclusions from the simulations:

- When the rotor becomes totally unstable, the system bifurcates from the *gyroscopic conical forward mode* (*3. Subsynchronous*) into the *gyroscopic forward mode 2 of Appendix B.2* (*gyroscopic forward mode 2 of Appendix B.3* in Simulation 4).
- Note that although bearing eccentricities $\varepsilon_{i,o}$ are very large and almost 1 when the rotor is in the region of the *Total Instability*, from a mechanical point of view, oscillation in the *Total Instability* is also a "stable" self-excited limit cycle oscillation. So, strictly speaking the rotor bifurcates from a limit cycle with moderate bearing eccentricities (*3. Subsynchronous*) into a limit cycle with very high bearing eccentricities (*Total Instability*). Therefore, totally unstable just means: Too high bearing eccentricities for safe technical operation.

- It is not very easy to give a clear physical explanation why the system bifurcates from the *3. Subsynchronous* into the *Total Instability*, since the system is complex and behaves in a highly nonlinear manner. It is clear that when rotor speed is increased, ring speeds also increase. Moreover, the inner and outer bearing eccentricities steadily increase with higher rotor speeds. Due to the higher bearing eccentricities, stiffness of the fluid films is steadily increased and the damping behavior of the fluid films becomes progressively "harder", which leads to a reduction of the (mutual) damping of the inner/outer oil films. Also, the *whirl/whip* frequency of the outer oil films (*3. Subsynchronous*) rises continuously. At a certain rotor speed, the bearing eccentricities are large enough, the *whirl/whip* frequency of the outer oil films is high enough, and also the stiffness and damping characteristic of the fluid films have changed in such a way that the limit cycle (*3. Subsynchronous*) becomes unstable and the system bifurcates into *Total Instability*.
- In contrast to the *1., 2.* and *3. Subsynchronous*, it is difficult to judge which of the four oil films is responsible for the bifurcation into *Total Instability*. One possible explanation could be the following: Due to the increasing bearing eccentricities, the damping behavior of the outer oil films is successively reduced so that at a certain point, the damping behavior of the outer oil films is too low to sufficiently damp the inner oil films. As a consequence, the inner oil films also become unstable, so that both oil films are simultaneously unstable and the system bifurcates into the *Total Instability*. It should be stressed that this explanation is a mere assumption and cannot be substantiated. Perhaps, the best interpretation for the *Total Instability* is to simply consider *Total Instability* as a bifurcation of the rotor/bearing system as a whole without any focus on a specific fluid film.
- In Table 2, Simulations 4, 3, and 5 are compared. It is evident that the more unstable the system becomes ($4 \rightarrow 3 \rightarrow 5$), the higher the bearing eccentricities are (increased bearing stiffness, "harder" bearing damping) and the higher the *whirl/whip* frequency of the *3. Subsynchronous* is.

Table 2
Comparison of different system quantities at simulation time $t = 7000$ ms for Simulations 4, 3 and 5: mean value of bearing eccentricities, ring speeds, vibration amplitude of measurement point (y-displacement) and frequency of *3. Subsynchronous*.

	Sim 4	Sim 3	Sim 5
Bearing eccentricity ε_{l_i}	0.1105	0.184	0.1909
Bearing eccentricity ε_{l_o}	0.7223	0.774	0.806
Bearing eccentricity ε_{r_i}	0.2919	0.3814	0.4126
Bearing eccentricity ε_{r_o}	0.8779	0.9	0.9108
Left ring speed ω_{R_l} (rad/ms)	1.598	1.517	1.457
Right ring speed ω_{R_r} (rad/ms)	1.22	1.186	1.150
Amplitude measurement point (mm)	0.288	0.3289	0.3939
Frequency of *3. Subsynchronous* (Hz)	131	139	139

The turbocharger investigated in this paper bifurcates from the *3. Subsynchronous* into the *Total Instability*. It is also imaginable that bifurcation into the *Total Instability* occurs as depicted in Fig. 12, namely from the *2. Subsynchronous* or from the *2./3. Subsynchronous*. However, the bifurcations sketched in Fig. 12 have not been observed with the actual rotor and the actual bearing parameters. Furthermore, it should be noted that the synchronized inner and outer *whirl/whip* may also excite higher normal modes (e.g., *gyroscopic forward mode 4 of Appendix B.2*), although this has not been detected with the current rotor.

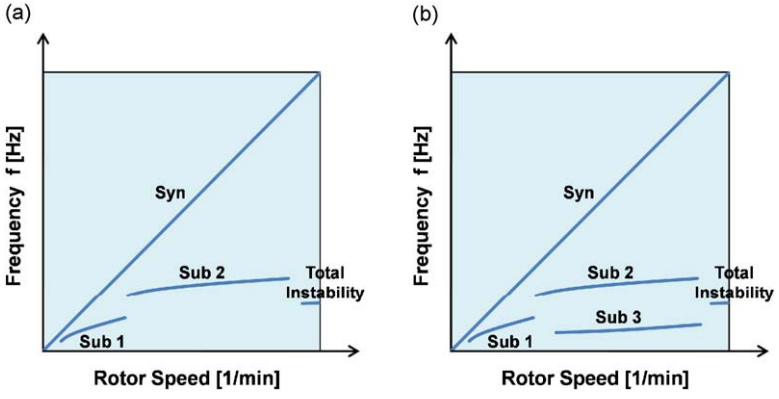

Fig. 12. Other possible bifurcation sequences into *Total Instability*: (a) bifurcation from Sub 2 into *Total Instability* and (b) bifurcation from Sub 2/Sub 3 into *Total Instability*.

4. Test-rig measurement of a rotor run-up

The run-up simulations are now compared with a corresponding measurement [32,33] carried out on a hot-gas turbocharger test rig, see Fig. 13(a). Hot gas, supplied through the hot gas pipe, sets the turbine wheel into rotation. Ambient air is compressed by the compressor wheel and exits the turbocharger through the charged air pipe. Lateral vibrations of the compressor-sided shaft extension are measured using eddy current sensors. The measurement starts at a rotor speed of $\approx$830 Hz. Rotor speed is steadily, but not uniformly increased.

Fig. 13(b) shows a 3D-waterfall diagram of the run-up measurement (y-displacement of the measurement point, see Fig. 4). The rotor becomes totally unstable at a rotor speed of approximately 1350 Hz; the instability frequency is approximately 280 Hz.

The measurement shows qualitatively and quantitatively the same behavior as Simulation 3:

(I) Before the *Total Instability* occurs, the rotor vibrates in the *3. Subsynchronous*.
(II) At a certain point, the rotor breaks out instantaneously with a frequency of approx. 280 Hz and becomes totally unstable. The vibration mode corresponds with the *gyroscopic forward mode 2 of Appendix B.2* (rotor in "stiff" bearings).

In the simulations, the rotor can be run in the region of the *Total Instability*. In the experiment, however, the rotor is immediately destroyed, when the rotor reaches *Total Instability*. Thus, the measurement cannot exhibit the same smooth spectra in the region of the *Total Instability* as the simulation.

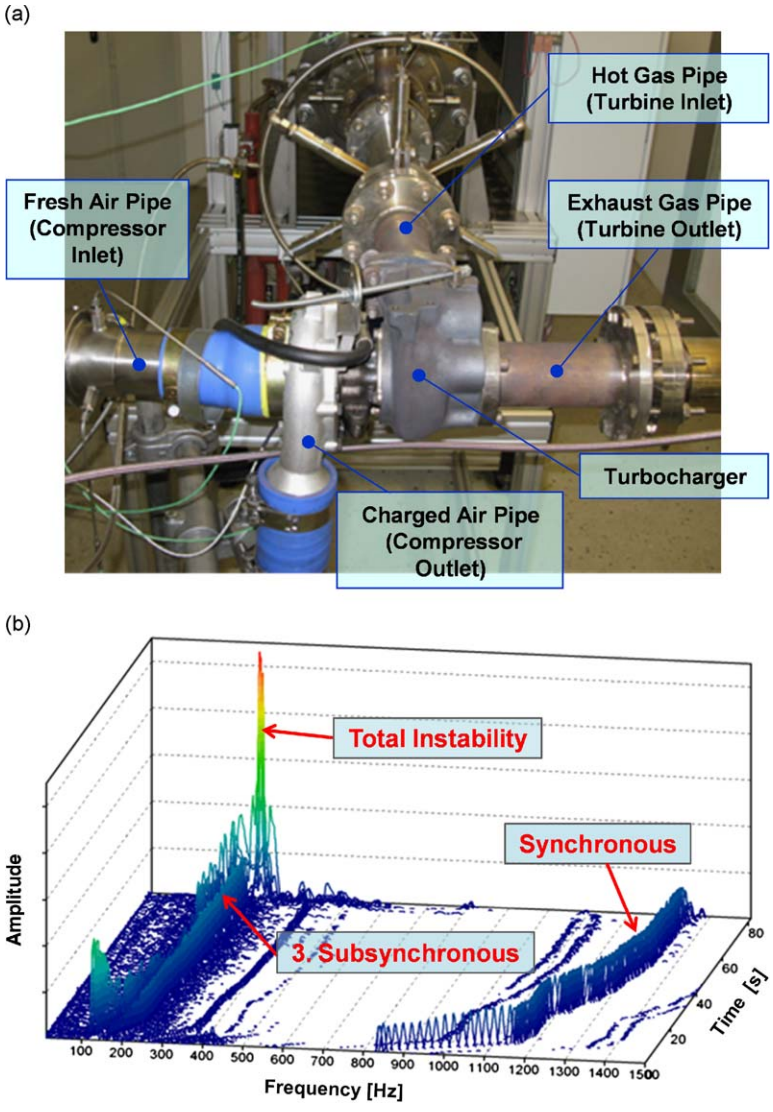

Fig. 13. (a) Hot-gas turbocharger test rig and (b) 3D-waterfall diagram of a run-up measurement (y-displacement of measurement point) exhibiting *Total Instability*.

5. Conclusions

The dynamic failure of turbocharger rotors supported in full-floating ring bearings, called *Total Instability* here, has been examined in this paper. It has been shown that the physical reason for *Total Instability* is based on a synchronization effect between the inner and outer *oil whirl/whip*, both simultaneously exciting the *gyroscopic forward mode 2 of Appendix B.2*.

The reason for *Total Instability* is not the mere simultaneous appearance of an unstable inner and outer fluid film, i.e., simultaneous inner and outer *oil whirl/whip*. Inner and outer fluid films can simultaneously be unstable—the *2. and 3. Subsynchronous* then appear simultaneously (see Fig. 2)—without leading to the *Total Instability*. In this case, inner and outer fluid films can damp each other sufficiently, because the *whirl/whip* frequencies of the inner (*2. Subsynchronous*) and the outer (*3. Subsynchronous*) fluid films are different, so that the inner fluid films damp the outer *whirl/whip* and vice versa due to $\dot{\varepsilon}_{i,o}$ and $\dot{\delta}_{i,o}$ damping. As a result, bearing eccentricities $\varepsilon_{i,o}$ remain clearly <1.

The situation becomes critical, if the inner and outer oil films simultaneously become unstable and if the inner and outer *whirl/whip* frequencies synchronize, so that both excite the same natural mode (here the *gyroscopic forward mode 2 of Appendix B.2*). Due to the *whirl/whip* synchronization, the mutual damping ($\dot{\varepsilon}_{i,o}$ and $\dot{\delta}_{i,o}$ damping) of the inner and outer fluid films is strongly reduced and the amplitudes $\varepsilon_{i,o}$ of the inner and outer *whirl/whip* almost reach 1.

In detail, the main results and conclusions of the numerical investigations are:

- Prior to bifurcation into *Total Instability*, the rotor oscillates in the *3. Subsynchronous*, which means that the *whirl/whip* frequency of the unstable outer fluid films excites the *gyroscopic conical forward mode* (Appendix B.1).
- In the simulations that reveal *Total Instability*, the inner and outer bearing eccentricities $\varepsilon_{i,o}$ successively increase with increasing rotor speed when the rotor oscillates in the *3. Subsynchronous*.
- When the bearing eccentricities increase even more, the stiffness and damping characteristic of the inner and outer fluid films change. Higher bearing eccentricities lead to increased bearing stiffnesses and cause a hardening of the fluid film damping. Thus, the damping behavior of the inner and outer fluid films is reduced more and more.
- Increasing ring speeds, stiffening/hardening of the fluid films, and gyroscopic effects entail an increase of the frequency of the *3. Subsynchronous*, when rotor speed rises.
- When the threshold speed is reached—i.e., the bearing eccentricities are high enough, stiffening/hardening of the inner and outer fluid films is large enough, and the ring speeds and the outer *whirl/whip* frequency are high enough—, the limit cycle oscillation in the *3. Subsynchronous* becomes unstable and the system bifurcates from the *3. Subsynchronous* into the *Total Instability*.
- At the onset of *Total Instability*, the inner fluid films become unstable, too.
- In the region of *Total Instability*, inner and the outer fluid films are simultaneously unstable, and their synchronized *whirl/whip* frequencies both excite the *gyroscopic forward mode 2 of Appendix B.2*.
- When the *whirl/whip* of the inner and outer fluid films have synchronized, this results in a strong reduction of the mutual damping between the inner and outer fluid film.
- Due to the loss of mutual damping in the *Total Instability*, inner and outer bearing eccentricities $\varepsilon_{i,o}$ are very large (close to 1). Furthermore, rotor amplitudes become extremely large.

Increasing imbalance, outer bearing clearance and inner bearing width as well as decreasing outer bearing width and oil supply pressure decreased the threshold speed of *Total Instability* for the examined rotor.

Appendix A

Some basic geometric and kinematic relationships concerning hydrodynamic bearings are recapitulated in Appendix A.

A.1. Plain hydrodynamic bearing

First, we consider a plain hydrodynamic journal bearing [29,30], consisting of a rotor journal (radius r, center M_J) and a bearing shell (radius $R = D/2$, fixed center M_S), see Fig. 14. Let x and y be the coordinates of a space-fixed coordinate system, whose origin coincides with M_S. The coordinates of the position vector to M_J with respect to the x, y-coordinate system are denoted by D_{Jx} and D_{Jy}. The time derivatives of D_{Jx} and D_{Jy} yield the coordinates of the velocity vector of M_J

$$V_{Jx} = \frac{\mathrm{d}}{\mathrm{d}t} D_{Jx} = \dot{D}_{Jx}, \quad V_{Jy} = \frac{\mathrm{d}}{\mathrm{d}t} D_{Jy} = \dot{D}_{Jy}. \tag{A.1}$$

$\mathrm{d}/\mathrm{d}t(\bullet)$ denotes the time derivative with respect to the x, y-coordinate system. The angular velocity of the rotor journal is represented by ω_J and the angular velocity of the bearing shell by ω_S. The width of the bearing in axial direction is denoted by B. $\psi = (R - r)/R$ defines the relative radial clearance of the bearing and $H(\varphi) = 1 + \varepsilon \cdot \cos(\varphi)$ the gap function (journal

misalignment is not considered). A polar coordinate system with the unit vectors

$$\mathbf{e}_r = \frac{1}{\sqrt{D_{Jx}^2 + D_{Jy}^2}} \begin{pmatrix} D_{Jx} \\ D_{Jy} \end{pmatrix}, \quad \mathbf{e}_\delta = \frac{1}{\sqrt{D_{Jx}^2 + D_{Jy}^2}} \begin{pmatrix} -D_{Jy} \\ D_{Jx} \end{pmatrix} \tag{A.2}$$

moves with the line of minimum film thickness, which is characterized by the angle δ. The dimensionless bearing eccentricity and its time derivative are determined by

$$\varepsilon = \frac{\sqrt{D_{Jx}^2 + D_{Jy}^2}}{R \cdot \psi}, \quad \dot{\varepsilon} = \frac{V_{Jx} \cdot D_{Jx} + V_{Jy} \cdot D_{Jy}}{R \cdot \psi \cdot \sqrt{D_{Jx}^2 + D_{Jy}^2}}. \tag{A.3}$$

The angular velocity of the line of minimum film thickness is given by

$$\dot{\delta} = \frac{-V_{Jx} \cdot D_{Jy} + V_{Jy} \cdot D_{Jx}}{(D_{Jx}^2 + D_{Jy}^2)}. \tag{A.4}$$

The effective hydrodynamic angular velocity is defined by

$$\omega_{\text{eff}} = (\omega_J + \omega_S - 2\dot{\delta}). \tag{A.5}$$

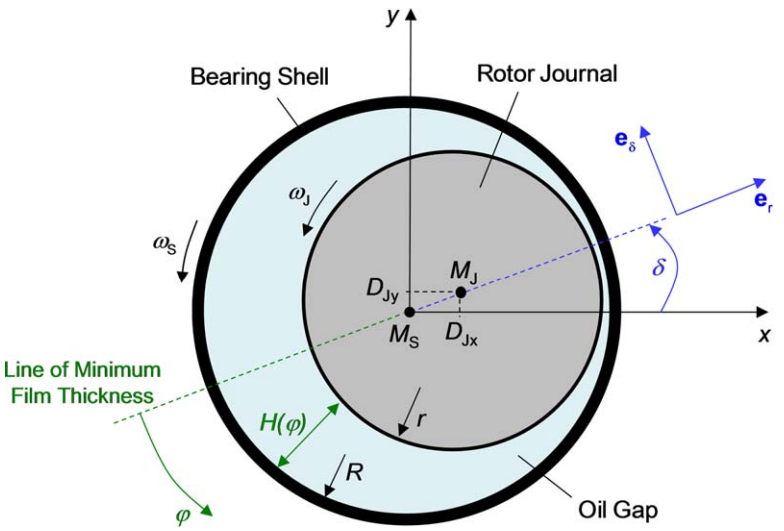

Fig. 14. Geometry of a plain hydrodynamic journal bearing.

A.2. Full-floating ring bearing

The above relationships are now extended for the floating ring bearing, see Fig. 15. Let *x,y* be the coordinates of a space-fixed coordinate system. With

- D_{Jx}, D_{Jy}: center of the rotor journal with respect to the *x*, *y*-coordinate system,
- D_{Rx}, D_{Ry}: center of the floating ring with respect to the *x*, *y*-coordinate system,
- D_{Sx}, D_{Sy}: center of the bearing shell with respect to the *x*, *y*-coordinate system,

one obtains for the inner gap

- $D_{x\_i} = D_{Jx} - D_{Rx}, D_{y\_i} = D_{Jy} - D_{Ry}$: relative displacement coordinates of the inner fluid gap,
- $V_{x\_i} = \dot{D}_{Jx} - \dot{D}_{Rx}, V_{y\_i} = \dot{D}_{Jy} - \dot{D}_{Ry}$: relative velocity coordinates of the inner fluid gap,

and for the outer gap

- $D_{x\_o} = D_{Rx} - D_{Sx}, D_{y\_o} = D_{Ry} - D_{Sy}$: relative displacement coordinates of the outer fluid gap,
- $V_{x\_o} = \dot{D}_{Rx} - \dot{D}_{Sx}, V_{y\_o} = \dot{D}_{Ry} - \dot{D}_{Sy}$: relative velocity coordinates of the outer fluid gap.

The unit vectors of the inner and outer polar coordinate system can be calculated by

$$\mathbf{e}_{r\_i,o} = \frac{1}{\sqrt{D_{x\_i,o}^2 + D_{y\_i,o}^2}} \begin{pmatrix} D_{x\_i,o} \\ D_{y\_i,o} \end{pmatrix}, \quad \mathbf{e}_{\delta\_i,o} = \frac{1}{\sqrt{D_{x\_i,o}^2 + D_{y\_i,o}^2}} \begin{pmatrix} -D_{y\_i,o} \\ D_{x\_i,o} \end{pmatrix}. \tag{A.6}$$

Bearing eccentricities of the inner and outer oil gap and the corresponding time derivatives are calculated by

$$\varepsilon_{i,o} = \frac{\sqrt{D_{x\_i,o}^2 + D_{y\_i,o}^2}}{R_{i,o} \cdot \psi_{i,o}}, \quad \dot{\varepsilon}_{i,o} = \frac{V_{x\_i,o} \cdot D_{x\_i,o} + V_{y\_i,o} \cdot D_{y\_i,o}}{R_{i,o} \cdot \psi_{i,o} \cdot \sqrt{D_{x\_i,o}^2 + D_{y\_i,o}^2}}. \tag{A.7}$$

Time derivative of the line of minimum film thickness of the inner and outer oil gap is given by

$$\dot{\delta}_{i,o} = \frac{-V_{x\_i,o} \cdot D_{y\_i,o} + V_{y\_i,o} \cdot D_{x\_i,o}}{(D_{x\_i,o}^2 + D_{y\_i,o}^2)}. \tag{A.8}$$

The angular velocity of the ring is denoted by ω_R. For the effective hydrodynamic angular velocities of the inner and outer oil gaps, one gets

$$\omega_{\text{eff\_}i} = (\omega_J + \omega_R - 2\dot{\delta}_i), \quad \omega_{\text{eff\_}o} = (\omega_R + \underbrace{\omega_S}_{=0} - 2\dot{\delta}_o) = (\omega_R - 2\dot{\delta}_o). \tag{A.9}$$

It should be noted that ω_S is assumed to be zero throughout this paper.

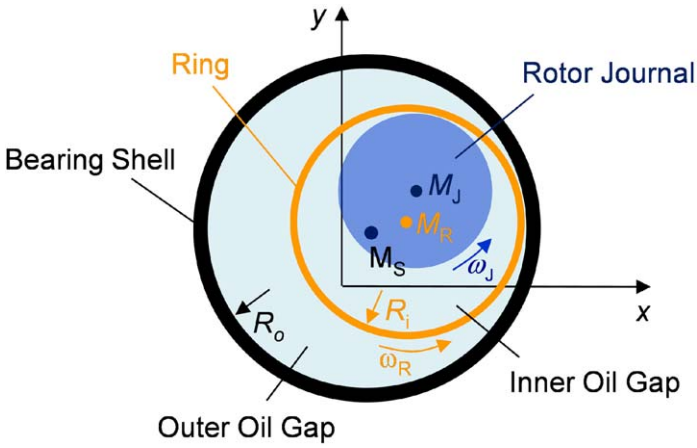

Fig. 15. Geometry of a full-floating ring bearing.

A.3. Hydrodynamic bearing forces

Solving Reynolds equation for the inner and outer oil films enables the resultant bearing forces to be calculated. The bearing forces can be subdivided into position-dependent ($\varepsilon_{i,o}$, $\delta_{i,o}$) and velocity-dependent ($\dot{\varepsilon}_{i,o}$, $\dot{\delta}_{i,o}$) forces [29,30]. The former are nonlinear "spring forces" and the latter nonlinear "damping forces". Therefore, fluid films primarily show two damping mechanisms:

- damping due to $\dot{\varepsilon}_{i,o}$ movement and
- damping due to $\dot{\delta}_{i,o}$ movement.

Appendix B

A gyroscopic eigenfrequency analysis of the rotor/bearing system gives information on the system's natural frequencies as a function of the rotor speed. To perform an eigenvalue analysis, the system has to be linearized. Therefore, the floating ring bearings in the multibody model of Section 2 have been linearized, simply by replacing them with linear springs acting in the x- and y-direction (assumed constant spring stiffness $c_{\text{res},x}$ and $c_{\text{res},y}$, see Fig. 16). In order to simplify matters,

bearing damping has been neglected in all eigenvalue analyses of Appendix B. The resultant stiffnesses $c_{res,x}$ and $c_{res,y}$ are defined by

- the stiffness of the inner fluid film,
- the stiffness of the outer fluid film and
- the stiffness of the bearing housing (including the elasticity of the floating ring).

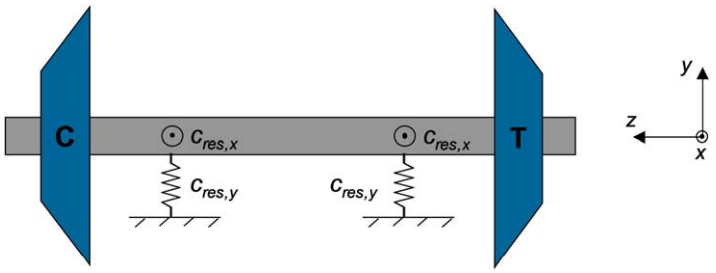

Fig. 16. Linear rotor/bearing model.

The three contributions to the resultant stiffness are arranged serially. As a consequence, if the bearing eccentricities are not too large (clearly less than 1), the stiffnesses of the inner and outer fluid films are clearly lower than the stiffness of the bearing housing and the ring. In this case, the resultant stiffness is dominated by the two fluid films, so that the stiffness of the bearing housing and the ring can approximately be set to infinity. If, on the other hand, the bearing eccentricities of both oil films are large (almost 1, as in the case of *Total Instability*), the fluid films are very stiff and the stiffness of the bearing housing and ring must be taken into account when calculating the resultant stiffness.

In Appendix B, three eigenvalue calculations are carried out, which only differ by choosing different values for the resultant spring stiffnesses $c_{res,x}$ and $c_{res,y}$.

B.1. Eigenvalue analysis 1

The resultant spring stiffnesses are assumed to be $c_{res,x} = c_{res,y} = 3000$ (N/mm) for both, the compressor-sided and the turbine-sided floating ring bearing. This corresponds to the case that the bearing eccentricities are not too large (clearly less than 1) and stiffness of bearing housing and ring can approximately be set to infinity. Fig. 17 shows the calculated normal modes.

- The first two natural modes are *rigid body conical modes* (elastic shaft bending is small): The first mode is the *gyroscopic conical reverse mode*, the second mode is the *gyroscopic conical forward mode*.
- The third and fourth natural mode are approximately *rigid body translational modes* (elastic shaft bending is little higher compared with the conical modes): The third mode is the *gyroscopic translational reverse mode* and the fourth mode is the *gyroscopic translational forward mode*.
- The fifth mode is the *first torsional mode*, which is not affected by gyroscopic effects and bearing stiffnesses.
- The sixth and seventh natural mode are *elastic bending modes*: The sixth mode is the *gyroscopic bending reverse mode*, the seventh mode is the *gyroscopic bending forward mode*.
- All modes—with exception of the torsional mode—are spatial modes (almost circular orbits already at low rotor speeds).

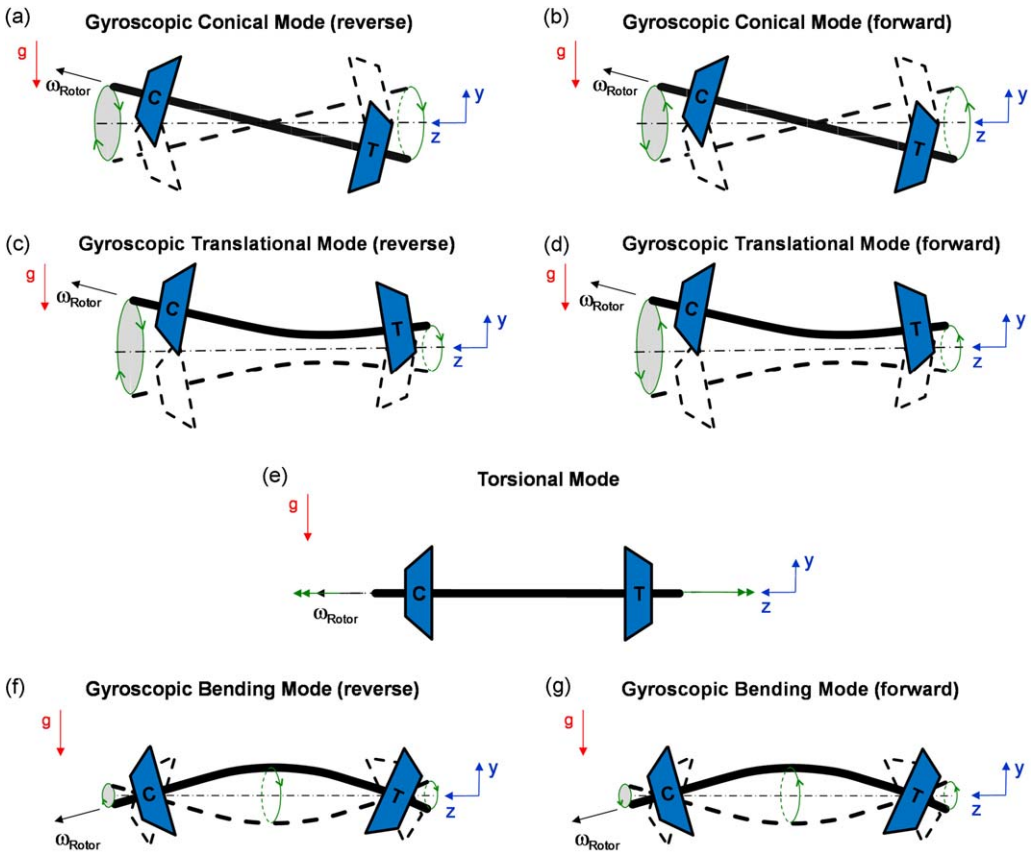

Fig. 17. Gyroscopic mode shapes of the turbocharger rotor in linear bearings with $c_{res,x} = c_{res,y} = 3000\,(\mathrm{N/mm})$ at a rotor angular velocity of $\omega_{Rotor} = 8000\,(\mathrm{rad/s})$: (a)–(g) gyroscopic reverse and forward modes.

The gyroscopic natural frequencies of the rotor at a rotor speed of 76 400 rev/min are:

- *Mode 1* (conical reverse): 60 Hz
- *Mode 2* (conical forward): 160 Hz
- *Mode 3* (translational reverse): 190 Hz
- *Mode 4* (translational forward): 255 Hz
- *Mode 5* (torsional): 580 Hz
- *Mode 6* (bending reverse): 400 Hz
- *Mode 7* (bending forward): 1420 Hz

Due to gyroscopic effects, the rotor's natural frequencies change when rotor speed is increased. Development of the system's eigenfrequencies with increasing rotor speed is shown in Fig. 18.

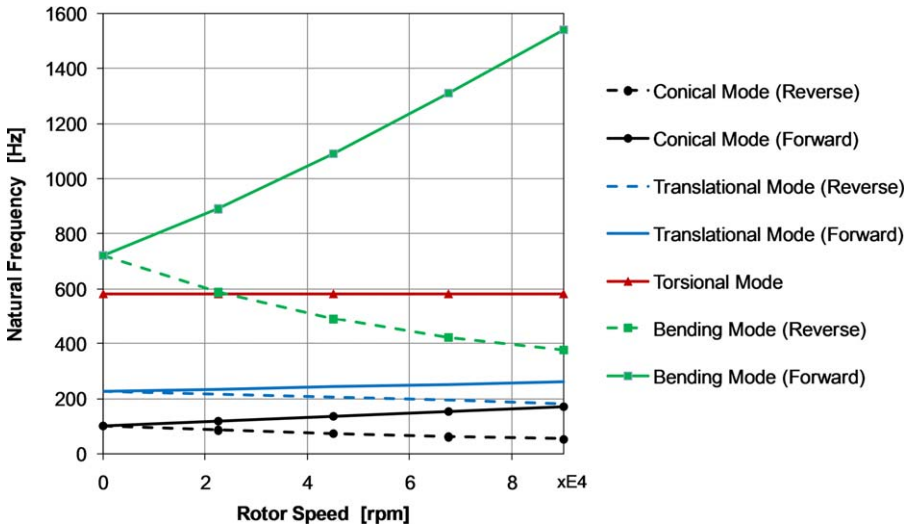

Fig. 18. Natural frequencies of the turbocharger rotor in linear bearings over the rotor speed.

Remark on the determination of $c_{res,x}$ and $c_{res,y}$: Replacing the highly nonlinear floating ring bearings with linear springs over the whole speed range is certainly not correct. In a wide rotor speed range, the rotor performs complex self-excited vibrations so that, strictly speaking, a linearization is not possible. For estimating $c_{res,x}$ and $c_{res,y}$, several run-up simulations with different rotor/bearing parameters have been performed in order to determine "mean bearing forces" and "mean shaft displacements". The ratio of "mean bearing forces" to "mean shaft displacements" yields a value of ≈ 3000 N/mm, which has been used as equivalent spring stiffness. The presented eigenvalue analyses should be considered qualitatively rather than quantitatively.

B.2. Eigenvalue analysis 2

The resultant spring stiffnesses are now assumed to be $c_{res,x} = c_{res,y} = 1.5\text{E}4$ (N/mm) for both the left and the right bearing. This corresponds to the case that the bearing eccentricities are large (e.g., when the rotor is *totally unstable*), so that stiffness of bearing housing and ring must be taken into account for calculating the resulting bearing stiffnesses. Fig. 19 shows the calculated normal modes.

- The first two natural modes "resemble" the *rigid body conical modes*, but due to the stiff bearings, elastic shaft bending is significantly larger. *Gyroscopic mode 1* is a reverse mode, *gyroscopic mode 2* is the corresponding forward mode.
- The third and fourth natural mode "resemble" the *rigid body translational modes*, but due to the stiff bearings, elastic shaft bending is significantly larger. *Gyroscopic mode 3* is a reverse mode, *gyroscopic mode 4* is the corresponding forward mode.
- The fifth mode is the *first torsional mode*.
- The sixth and seventh natural mode are *gyroscopic bending modes* with two vibration nodes: *gyroscopic mode 6* is a reverse mode, *gyroscopic mode 7* is the corresponding forward mode.
- The eighth natural mode is an *elastic bending mode* with three vibration nodes (S-shaped): *gyroscopic mode 8* is a reverse mode. The corresponding forward mode is not shown in Fig. 19.
- All modes—with the exception of the torsional mode—are spatial modes.

The gyroscopic natural frequencies of the rotor at a rotor speed of 76 400 rev/min are:

- *Gyroscopic mode 1* (reverse): 125 Hz
- *Gyroscopic mode 2* (forward): 270 Hz
- *Gyroscopic mode 3* (reverse): 230 Hz
- *Gyroscopic mode 4* (forward): 420 Hz
- *Gyroscopic mode 5* (torsional): 580 Hz
- *Gyroscopic mode 6* (reverse): 850 Hz
- *Gyroscopic mode 7* (forward): 1760 Hz
- *Gyroscopic mode 8* (reverse): 1665 Hz

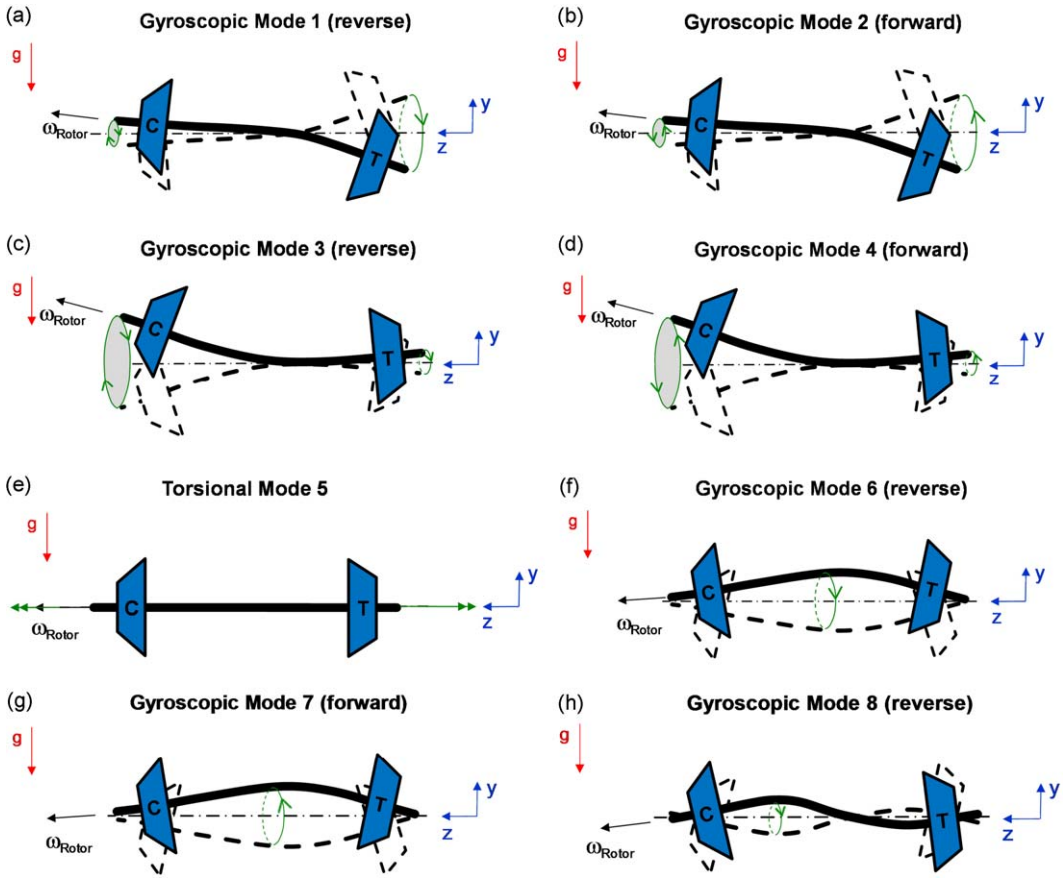

Fig. 19. Gyroscopic mode shapes of the turbocharger rotor in linear bearings with $c_{res,x} = c_{res,y} = 1.5E4\,(N/mm)$ at a rotor angular velocity of $\omega_{Rotor} = 8000\,(rad/s)$. (a)–(g) Gyroscopic reverse and forward modes.

B.3. Eigenvalue analysis 3

In contrast to eigenvalue analysis 2, the resulting bearing stiffnesses are further increased and assumed to be $c_{res,x} = c_{res,y} = 1.5E5\,(N/mm)$. This corresponds to the case of very stiff, almost rigid bearings. Eigenvalue analysis 3 is carried out in order to show that housing stiffness may be important for calculating the accurate instability mode and frequency when the rotor gets totally unstable (see Simulation 4 in Section 3). Fig. 20 shows the calculated normal modes.

- *Gyroscopic mode 1* is a reverse mode and *gyroscopic mode 2* is the corresponding forward mode. Both are elastic modes, where the amplitudes of the turbine wheel are larger than the amplitudes of the compressor wheel.
- *Gyroscopic mode 3* is a reverse mode and *gyroscopic mode 4* is the corresponding forward mode. Both are elastic modes, where the amplitudes of the turbine wheel are smaller than the amplitudes of the compressor wheel.
- The fifth mode is the *first torsional mode*.
- *Gyroscopic mode 6* is a reverse mode with large elastic bending located at the turbine wheel. The corresponding forward mode is not depicted in Fig. 20.

The gyroscopic natural frequencies of the rotor at a rotor speed of 76 400 rev/min are:

- *Gyroscopic mode 1* (reverse): 170 Hz
- *Gyroscopic mode 2* (forward): 430 Hz
- *Gyroscopic mode 3* (reverse): 330 Hz
- *Gyroscopic mode 4* (forward): 615 Hz
- *Gyroscopic mode 5* (torsional): 580 Hz
- *Gyroscopic mode 6* (reverse): 2310 Hz

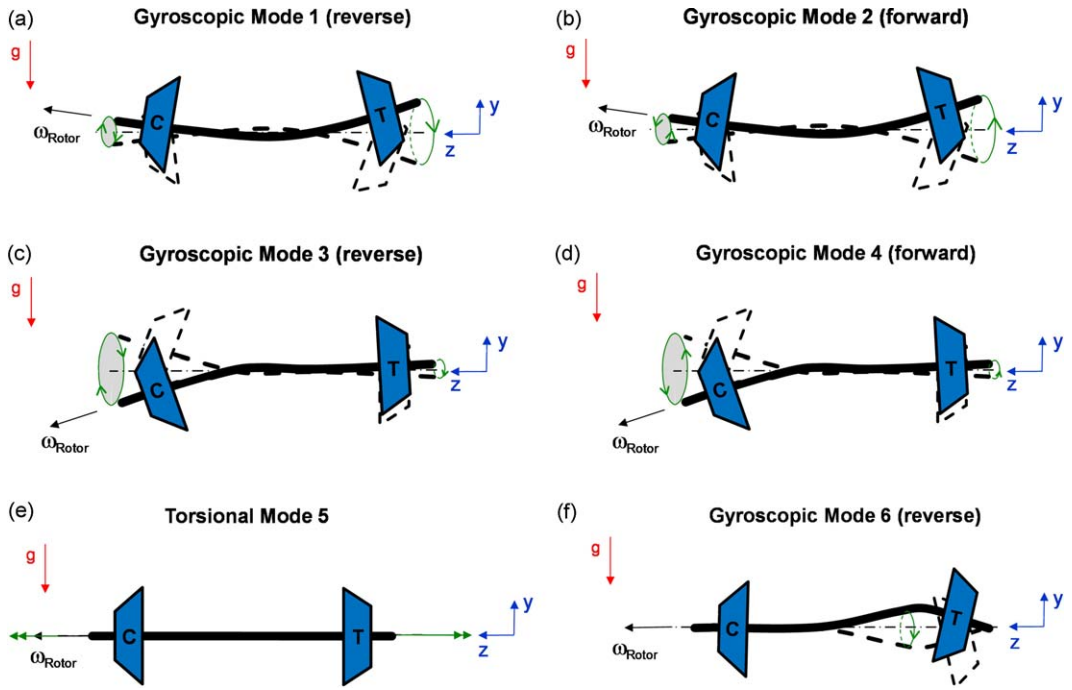

Fig. 20. Gyroscopic mode shapes of the turbocharger rotor in linear bearings with $c_{res,x} = c_{res,y} = 1.5E5\,(N/mm)$ at a rotor angular velocity of $\omega_{Rotor} = 8000\,[rad/s]$: (a)–(g) gyroscopic reverse and forward modes.

Appendix C

C.1. *Laval rotor in single oil film bearings*

Oil whirl/whip instabilities play a crucial role in the dynamics of turbochargers. Therefore, the stability behavior of a Laval (Jeffcott) rotor during a rotor run-up is shortly recapitulated. The rotor (rotor mass $m = 0.1\,kg$, rotor imbalance $U_R = 0.4\,gmm$, shaft stiffness $c_{shaft} = 2000\,N/mm$, internal shaft damping $d_{shaft} = 0\,Ns/m$) is symmetrically supported in two plain hydrodynamic journal bearings (bearing diameter $D = 6.0\,mm$, bearing width $B = 3.6\,mm$, relative bearing clearance $\psi = 3.8E-3$, oil viscosity $\eta = 0.01\,Ns/m^2$), see Fig. 21(a). An external, linear damping force is applied at the rotor center M_C according to

$$\mathbf{F}_{d,ex} = -d_{ex}\begin{pmatrix} V_{Cx} \\ V_{Cy} \end{pmatrix}, \tag{C.1}$$

where V_{Cx} and V_{Cy} denote the coordinates of the translational velocity of M_C.

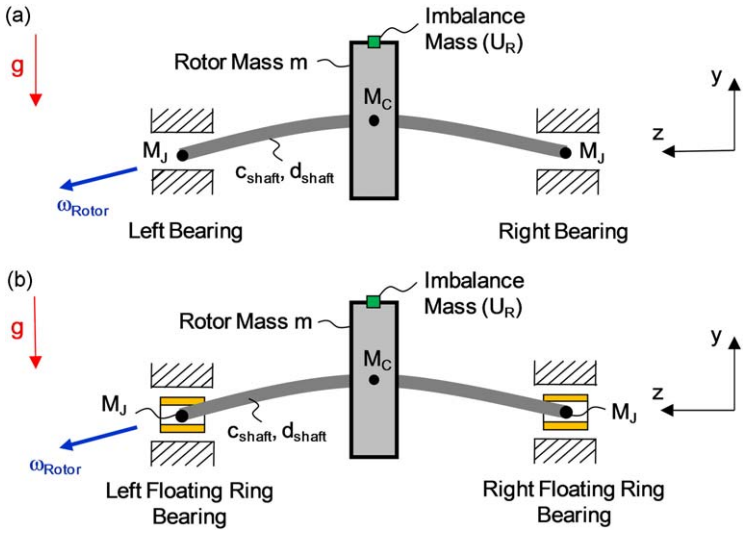

Fig. 21. Laval rotor symmetrically supported: (a) in plain hydrodynamic journal bearings and (b) in full-floating ring bearings.

During the run-up, rotor speed ω_{Rotor} is steadily increased starting from zero angular velocity up to 4000 Hz. Fig. 22 depicts the motion of the rotor center M_C and the rotor journal M_J as well as the bearing eccentricity ε and the effective hydrodynamic angular velocity ω_{eff}.

- Below the threshold speed of instability, the rotor performs imbalance vibrations around a stable equilibrium position (note the rotor resonance at $t \approx 2700$ ms).
- The rotor becomes unstable (*oil whirl/whip*) at $t \approx 3700$ ms.
- Due to the applied external damping, *oil whirl/whip* instability can be passed through and the rotor becomes stable again at $t \approx 5900$ ms.

Remark: Throughout this paper, the rotor (oil film) is said to become unstable, if the bearing eccentricities sharply increase. However, the transition from stable imbalance vibrations to the region of complete instability (fully developed *oil whirl/whip* region) can be rather complicated [25,34], so that one strictly should distinguish between "threshold speed of instability" and "region of complete instability" (fully developed *oil whirl/whip* region), which is not done in the present paper.

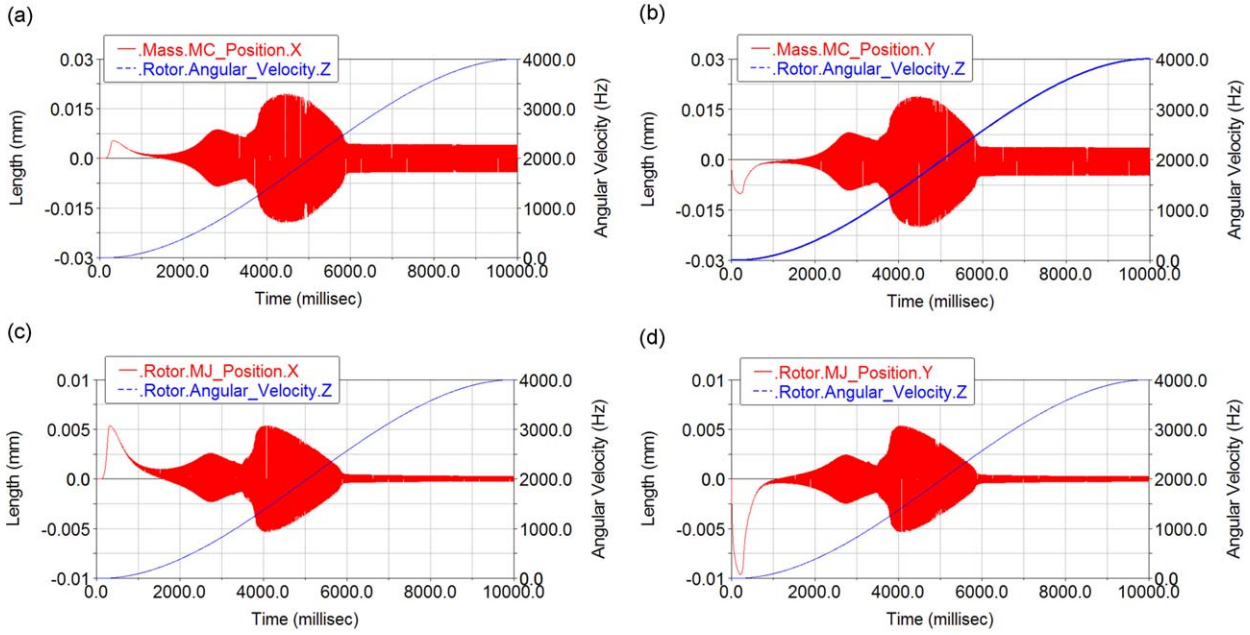

Fig. 22. Run-up simulation of a Laval rotor in single oil film bearings ($m = 0.1$ kg, $c_{\text{shaft}} = 2000$ N/mm, $U_R = 0.4$ gmm, $d_{\text{ex}} = 90$ Ns/m, $d_{\text{shaft}} = 0$ Ns/m): (a, b) x- and y-position of mass center M_C and rotor speed, (c, d) x- and y-position of rotor journal M_J, (e) 3D-waterfall diagram of plot (a), (f) top-view waterfall diagram, (g) bearing eccentricity ε and (h) effective hydrodynamic angular velocity ω_{eff}.

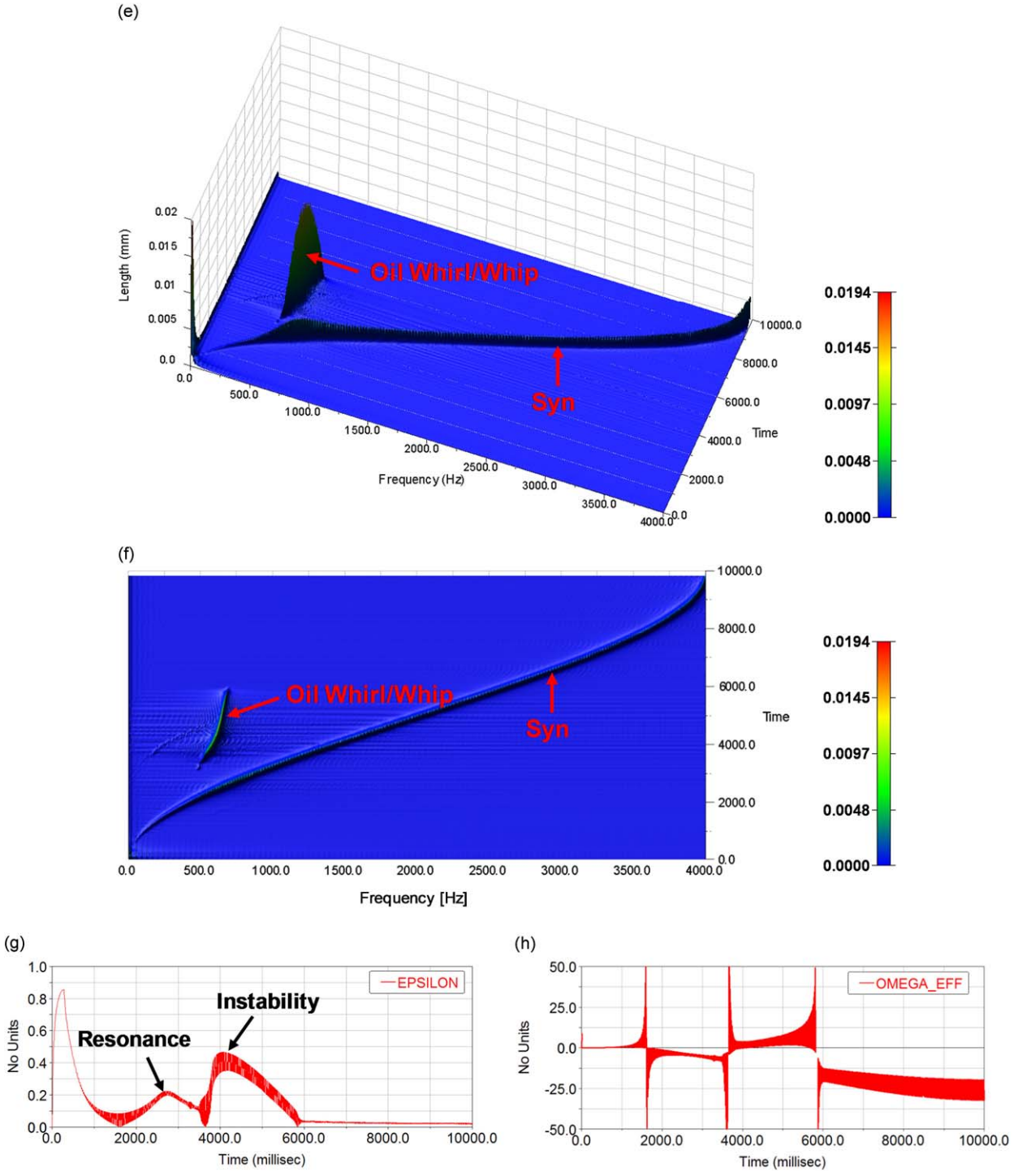

Fig. 22. (*Continued*)

C.2. Laval rotor in full-floating ring bearings

C.2.1. Laval rotor in full-floating ring bearings not exhibiting Total Instability

Fluid-film-induced instabilities and bifurcations occurring in rotors supported in full-floating ring bearings, see Fig. 21(b), are more complex than in the case of single oil film bearings [18,35]. A typical run-up simulation (0–4000 Hz in 10 000 ms) of a Laval rotor ($m = 0.1$ kg, $c_{\text{shaft}} = 3000$ N/mm, $d_{\text{shaft}} = 0$ Ns/m, $d_{\text{ex}} = 0$ Ns/m, $U_R = 0.2$ gmm) in full-floating ring bearings (inner/outer bearing diameter $D_i/D_o = 6$ mm/9.5 mm, inner/outer bearing width $B_i/B_o = 3.6$ mm/6.15 mm, relative inner/outer bearing clearance $\psi_i/\psi_o = 3.8\text{E}{-3}/6.7\text{E}{-3}$, inner/outer oil viscosity $\eta_i/\eta_o = 0.01\ \text{Ns/m}^2/0.015\ \text{Ns/m}^2$) is shown in Fig. 23. In full-floating ring bearings, both fluid films—the inner and the outer fluid film—may become unstable. Hence, one observes *oil whirl/whip* instabilities generated by the inner and outer fluid films.

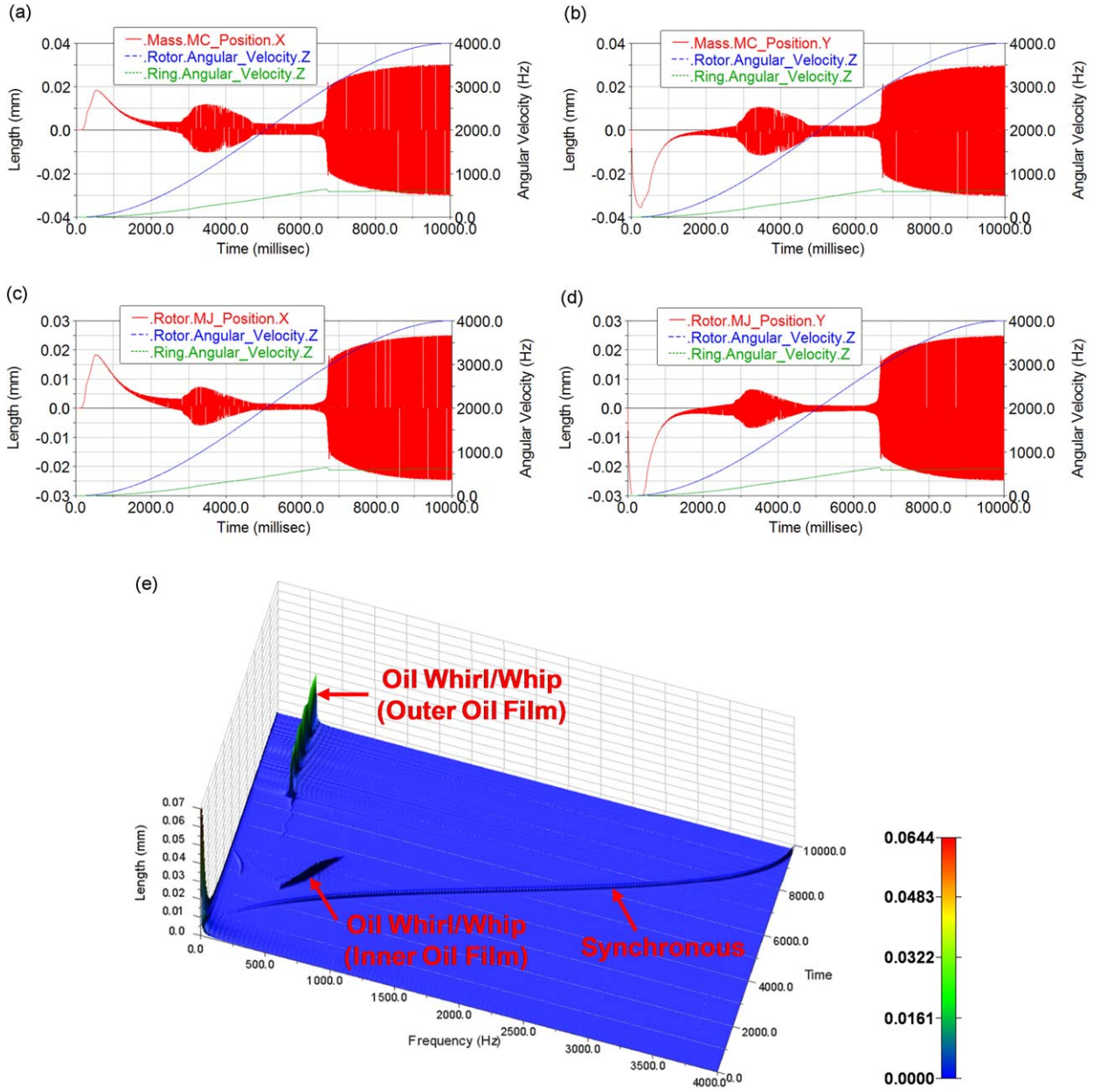

Fig. 23. Run-up simulation of a Laval rotor ($m = 0.1$ kg, $c_{\text{shaft}} = 3000$ N/mm, $U_R = 0.2$ gmm, $d_{\text{ex}} = d_{\text{shaft}} = 0$ Ns/m) in full-floating ring bearings (not reaching *Total Instability*): (a, b) x- and y-position of mass center M_C, rotor and ring speed. (c, d) x- and y-position of rotor journal M_J, (e) 3D-waterfall diagram of plot (a), (f) top-view waterfall diagram, (g) inner/outer bearing eccentricities and (h, i) inner/outer effective hydrodynamic angular velocities.

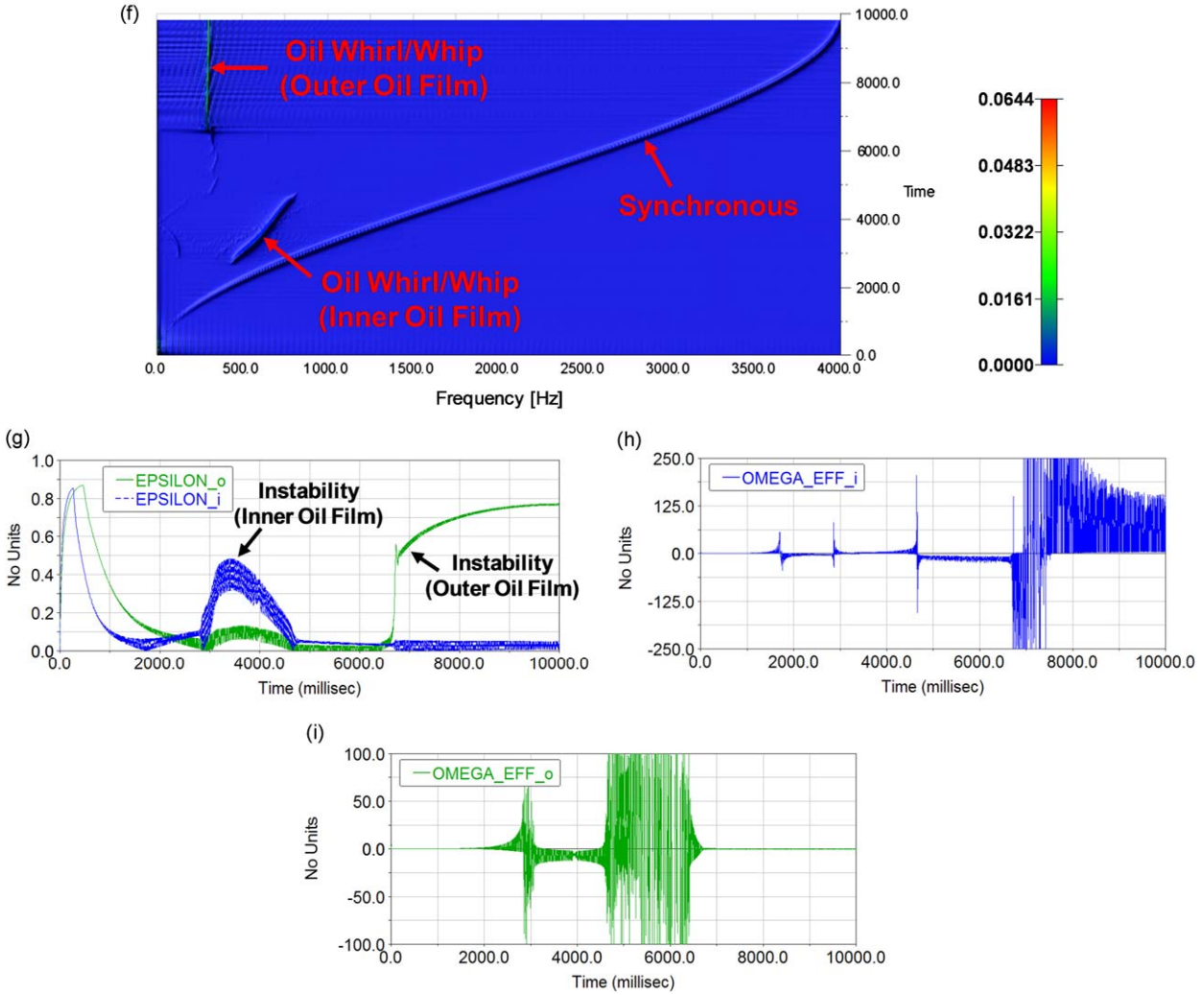

Fig. 23. (*Continued*)

- The inner fluid films become unstable at $t \approx 2900$ ms.
- The inner *oil whirl/whip* is passed through at $t \approx 4800$ ms.
- At higher rotor speeds ($t \approx 6700$ ms), the outer fluid films become unstable.

Note that although internal shaft damping and also external damping have been neglected, inner and outer bearing eccentricities $\varepsilon_{i,o}$ remain well below 1 in the *oil whirl/whip* region due to the (mutual) damping of the inner and outer fluid films (the outer oil films damp the inner *whirl/whip* and vice versa). Also, rotor amplitudes remain moderate in the *whirl/whip* regions.

C.2.2. Laval rotor in full-floating ring bearings exhibiting Total Instability

In contrast to single oil film bearings, full-floating ring bearings show a further kind of instability/bifurcation, namely the *Total Instability*. In Sections 3 and 4, *Total Instability* has been analyzed in turbocharger systems. *Total Instability* may also be observed in simple rotor systems [18]. To demonstrate this, we consider a Laval rotor ($m = 2$ kg, $c_{\text{shaft}} = 1.2\text{E}4$ N/mm, $d_{\text{ex}} = d_{\text{shaft}} = 0$ Ns/m, $U_R = 15$ gmm) symmetrically supported in two full-floating ring bearings (inner/outer bearing diameter $D_i/D_o = 18$ mm/25 mm, inner/outer bearing width $B_i/B_o = 10$ mm/10 mm, relative inner/outer bearing clearance $\psi_i/\psi_o = 5.25\text{E}{-3}/4.68\text{E}{-3}$, inner/outer oil viscosity $\eta_i/\eta_o = 6.4\text{E}{-3}$ Ns/m^2/$9.5\text{E}{-3}$ Ns/m^2). A run-up simulation (0–3000 Hz in 10 000 ms) shows the following results, see Fig. 24.

- The rotor is stable and performs imbalance vibrations around a stable equilibrium position up to $t \approx 3700$ ms.
- The outer oil films become unstable (outer *oil whirl/whip*) at $t \approx 3600$ ms. The inner fluid films remain stable.
- At $t \approx 7700$ ms, the outer *oil whirl/whip* becomes unstable and the rotor bifurcates into *Total Instability*. At the onset of *Total Instability*, the inner fluid films become unstable (note the large increase of ε_i) so that now both fluid films are simultaneously unstable. The rotor amplitudes suddenly increase and the subsynchronous frequency jumps into the resonance frequency $\omega_{\text{Eig}} = \sqrt{c_{\text{shaft}}/m} = 390$ Hz of the rotor, i.e., the system bifurcates into the rotor natural mode (due to the large bearing eccentricities, the fluid films are very stiff and the natural frequency of the rotor/bearing system is approximately ω_{Eig}).

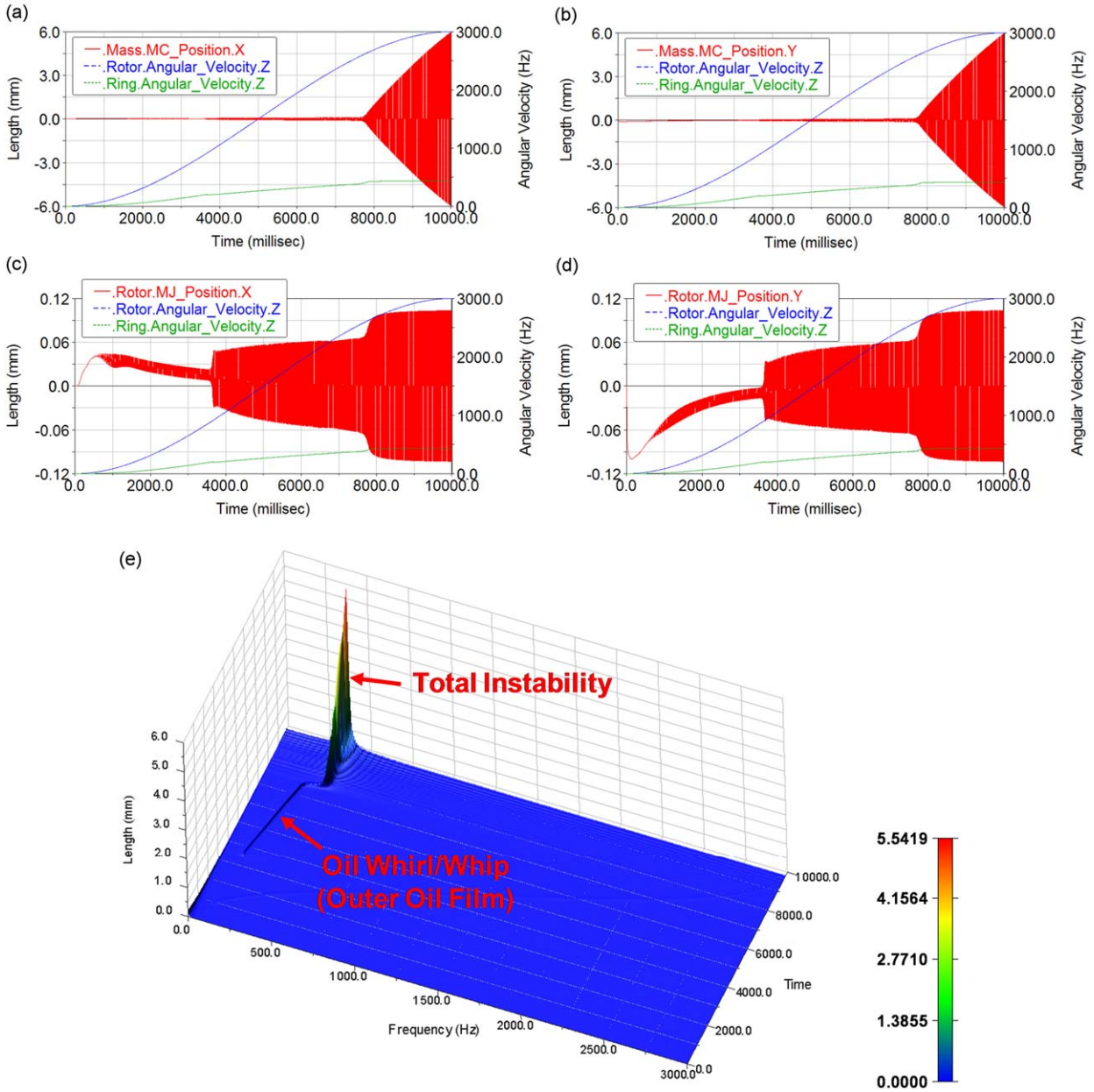

Fig. 24. Run-up simulation of a Laval rotor ($m = 2$ kg, $c_{\text{shaft}} = 12\,000$ N/mm, $U_R = 15$ gmm, $d_{\text{ex}} = d_{\text{shaft}} = 0$ Ns/m) in full-floating ring bearings (reaching *Total Instability*): (a, b) x- and y-position of mass center M_C, rotor and ring speed, (c, d) x- and y-position of rotor journal M_J, (e) 3D-waterfall diagram of plot (a), (f) top-view waterfall diagram, (g) inner/outer bearing eccentricities and (h, i) inner/outer effective hydrodynamic angular velocities.

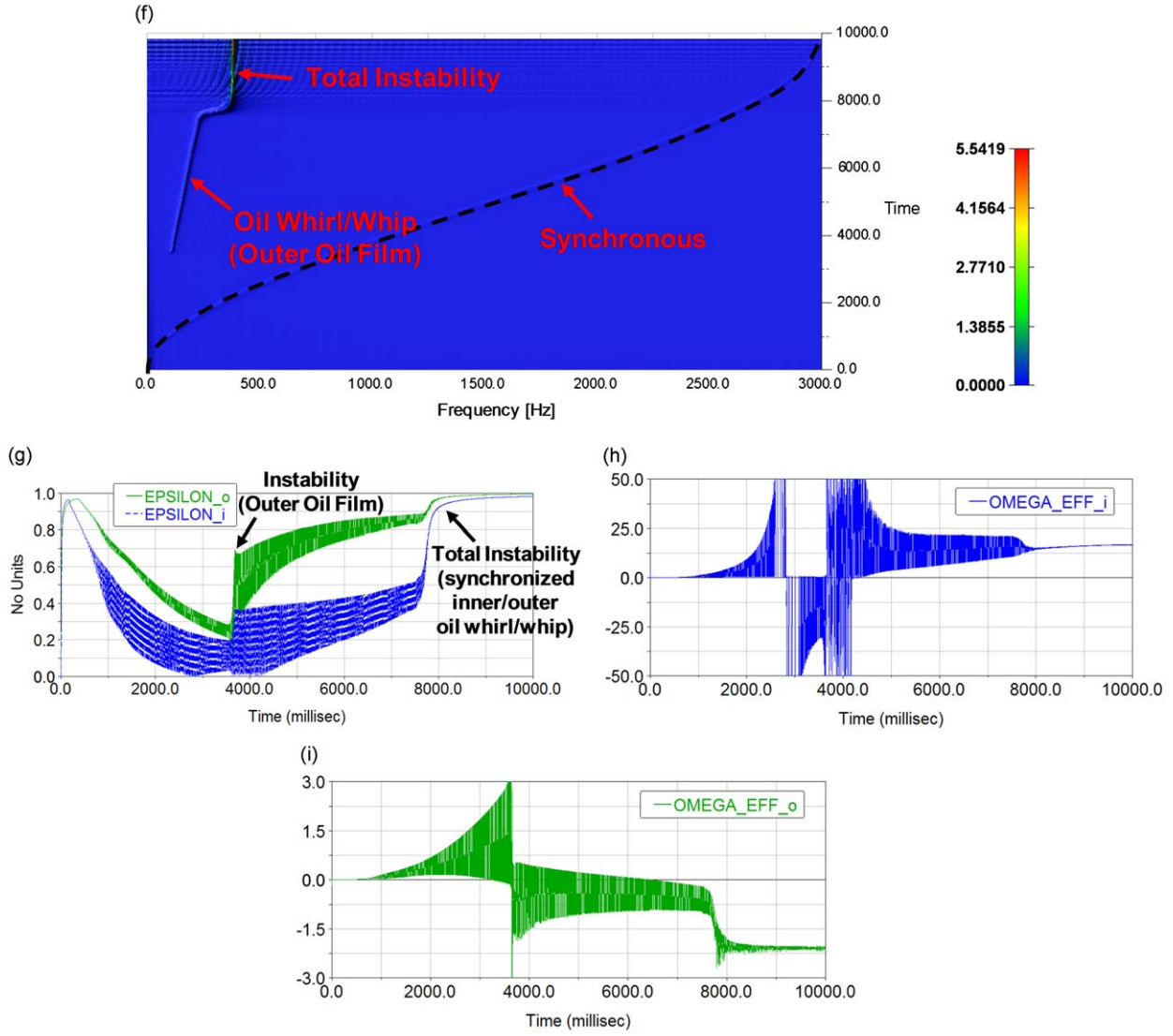

Fig. 24. (*Continued*)

As mentioned above, in rotors with full-floating ring bearings, inner and outer fluid films can simultaneously be unstable without leading to the *Total Instability*, if the inner and the outer *whirl/whip* frequencies are different. In this case, the inner and outer fluid films can damp each other mutually so that inner and outer bearing eccentricities $\varepsilon_{i,o}$ remain well below 1.

In the critical case of *Total Instability*, the inner and the outer *whirl/whip* frequency synchronize, and the common *whirl/whip* frequency excites the rotor natural mode (resonance frequency ω_{Eig}). Due to this synchronization, the mutual damping ($\dot{\varepsilon}_{i,o}$ and $\dot{\delta}_{i,o}$ damping) between the inner and outer oil films is strongly reduced. As a consequence, rotor amplitudes become very large and bearing eccentricities $\varepsilon_{i,o}$ reach almost 1.

When the Laval rotor bifurcates into *Total Instability*, quite similar effects can be observed as in the case of the turbocharger rotor. When the rotor speed is increased, the bearing eccentricities $\varepsilon_{i,o}$ continuously increase, which leads to a stiffening of the fluid films and a hardening of the oil film damping. Consequently, the damping behavior ($\dot{\varepsilon}_{i,o}$ and $\dot{\delta}_{i,o}$ damping) of the inner and outer fluid films is successively reduced. Also, the ring speed and the outer *oil whirl/whip* frequency steadily increase with increasing rotor speed. When the bearing eccentricities, the fluid film stiffening/hardening, and the outer *oil whirl/whip* frequency are high enough, the limit cycle (outer *oil whirl/whip*) becomes unstable and the system bifurcates into *Total Instability*.

References

[1] B. Schweizer, M. Sievert, Nonlinear oscillations of automotive turbocharger turbines, Journal of Sound and Vibration 321 (2009) 955–975, doi:10.1016/j.jsv.2008.10.013.
[2] A. Muszynska, J.W. Grant, Stability and instability of a two-mode rotor supported by two fluid-lubricated bearings, *Journal of Vibration and Acoustics* 113 (3) (1991) 316–324.
[3] Q. Ding, A.Y.T. Leung, Numerical and experimental investigations on flexible multi-bearing rotor dynamics, *Journal of Vibration and Acoustics* 127 (4) (2005) 408–415.
[4] A. Muszynska, The fluid force model in rotating machine clearances identified by modal testing and model applications: an adequate interpretation of the fluid-induced instabilities, *Proceedings of the International Symposium on Stability Control of Rotating Machinery*, Iscorma-2, South Lake Tahoe, 2001, CA, USA.
[5] T. Someya, Stabilität einer in zylindrischen Gleitlagern laufenden, unwuchtfreien Welle (Stability of a rotor without imbalance in plain hydrodynamic bearings), *Ingenieur-Archiv (Archive of Applied Mechanics)* 23 (1963) 85–108.
[6] T. Someya, Schwingungs- und Stabilitätsverhalten einer in zylindrischen Gleitlagern laufenden Welle mit Unwucht (*Vibrations and Stability Behavior of a Rotor with Imbalance in Plain Hydrodynamic Bearings*), VDI-Forschungsheft (VDI Research Book), Vol. 510, 1965.
[7] J.W. Lund, B. Sternlicht, Rotor bearing dynamics with emphasis on attenuation, *ASME Journal of Basic Engineering* 84 (1962) 491–502.
[8] J.W. Lund, Stability and damped critical speeds of a flexible rotor in fluid film bearings, *Journal of Engineering for Industry* (1974) 509–517.
[9] A. Muszynska, Whirl and whip—rotor/bearing stability problems, *Journal of Sound and Vibration* 110 (3) (1986) 443–462.
[10] A. Muszynska, Tracking the mystery of oil whirl, *Journal of Sound and Vibration* February (1987) 8–12.
[11] A. Muszynska, Stability of whirl and whip in rotor/bearing systems, *Journal of Sound and Vibration* 127 (1) (1988) 49–64.
[12] Z. Guo, R.G. Kirk, Instability boundary for rotor–hydrodynamic bearing systems—part 1: Jeffcott rotor with external damping, *Journal of Vibration and Acoustics* 125 (4) (2003) 417–422.
[13] Z. Guo, R.G. Kirk, Instability boundary for rotor-hydrodynamic bearing systems—part 2: rotor with external flexible damped support, *Journal of Vibration and Acoustics* 125 (4) (2003) 423–426.
[14] M. Tanaka, Y. Hori, Stability characteristics of floating bush bearings, *ASME Journal of Lubrication Technology* 94 (1972) 248–259.
[15] M. Tanaka, A theoretical analysis of stability characteristics of high-speed floating bush bearings, *IMechE Conference Transactions of Sixth International Conference on Vibrations in Rotating Machinery*, 1996, pp. 133–142.
[16] A. Tatara, An experimental study of the stabilizing effect of floating-bush journal bearings, *Bulletin of JSME* 13 (61) (1970) 858–863.
[17] R.J. Trippett, Measured and predicted friction in floating-ring bearings, *SAE Transactions* 95 (1986) 1470–1476.
[18] B. Schweizer, Oil whirl, oil whip and whirl/whip synchronization occurring in rotor systems with full-floating ring bearings, *Journal of Nonlinear Dynamics*, 2009, Doi:10.1007/s11071-009-9466-3.
[19] C. Holt, L. San Andres, Test response and nonlinear analysis of a turbocharger supported on floating ring bearings, *Journal of Vibration and Acoustics* 127 (2005) 107–115.
[20] L. San Andrés, J.C. Rivadeneira, K. Gjika, C. Groves, G. LaRue, Rotordynamics of small turbochargers supported on floating ring bearings—highlights in bearing analysis and experimental validation, *ASME Journal of Tribology* 129 (2007) 391–397.
[21] B. Schweizer, Vibrations and bifurcations of turbocharger rotors, *Proceedings of the Eighth International Conference on Vibrations in Rotating Machines*, SIRM 2009, Paper-ID 12, ISBN 978-3-200-01412-1, Vienna, Austria, 23–25 February 2009.
[22] A.H. Nayfeh, D.T. Mook, *Nonlinear Oscillations*, Wiley-Interscience, New York, reprint edition 1995.
[23] P. Hagedorn, *Nonlinear Oscillations*, second ed., Oxford University Press, Clarendon Press, Oxford, 1988.
[24] J. Argyris, G. Faust, M. Haase, *An Exploration of Chaos*, North-Holland, Amsterdam, 1994.
[25] C.J. Myers, Bifurcation theory applied to oil whirl in plain cylindrical journal bearings, *ASME Journal of Applied Mechanics* 51 (1984) 244–250.
[26] J. Shaw, S.W. Shaw, The effects of unbalance on oil whirl, *Nonlinear Dynamics* (1990) 293–311.
[27] A. Boyaci, H. Hetzler, W. Seemann, C. Proppe, Analytical bifurcation analysis of a rotor supported by floating ring bearings, *Nonlinear Dynamics*, DOI:10.1007/s11071-008-9403-x.
[28] A. Shabana, *Dynamics of Multibody Systems*, Cambridge University Press, Cambridge, 2005.
[29] A. Cameron, *Basic Lubrication Theory*, Horwood, Chichester, 1981.
[30] M.M. Khonsari, E.R. Booser, *Applied Tribology*, second ed., Wiley, New York, 2008.
[31] R.R. Craig, M.C. Bampton, Coupling of substructures for dynamics analysis, *AIAA Journal* 6 (1968) 1313–1319.
[32] G. Knoll, B. Schweizer, K. Backhaus, J. Lang, U. Schmid, Multibody modelling of full floating ring bearings, *Proceedings of the Tribology Conference 2007*, Göttingen, Germany, 2007.
[33] W. Seemann, C. Proppe, G. Knoll, Multibody run-up simulation of turbocharger rotors in nonlinear modeled floating ring bearings, *Semi-Annual Congress Spring 2008*, Report No. R 542, Research Association Engine/Turbomachinery, Frankfurt/Main, Germany, 2008.
[34] J.K. Wang, M.M. Khonsari, Bifurcation analysis of a flexible rotor supported by two fluid-film journal bearings, *Journal of Tribology—Transactions of the ASME* 128 (3) (2006) 594–603.
[35] B. Schweizer, Dynamics and Stability of Turbocharger Rotors, Archive of Applied Mechanics, 2009, doi:10.1007/s00419-009-0331-0.